POLITECNICO DI TORINO

Master's Degree in Biomedical Engineering

Master's Degree Thesis

Evaluation of garlic derived carbon dots for citocompatibility and radical scavenging: from structure to properties

Supervisors:
Prof. Tagliaferro Alberto
Prof. Frascella Francesca
Dr. Bartoli Mattia

Candidate:
Ala Miriam

Academic Year 2023-2024

Contents

Abstract

Carbon dots are an emerging and fascinating carbon-based material, characterized by nearly spherical shapes with size lower than 10 nm, excellent optical properties and intense fluorescence. Carbon dots are suitable for various applications, like in optoelectronics, photocatalysis, sensing, and, particularly in the biomedical field. Thanks to their biocompatibility and low toxicity, they can be employed as drug and gene carriers, perform antioxidant actions, and are useful in theranostic applications. Their fluorescence capability allows them to act as chemical probes for detecting specific metallic ions and for bioimaging.

Another outstanding feature is the tunability of their properties. Tuning of the carbon dots properties can be achieved by tailoring their composition, chemical structure, and size within the range 10-80 nm. Carbon dots are organic nanoparticles and can be produced through various synthesis methodologies. In this thesis work, carbon dots were synthesized using biomass, specifically garlic, through a hydrothermal synthesis. This approach, classified as a bottom-up technique, involves a straightforward realization but incorporates a top-down approach by including the cutting of the starting biomass. Five different syntheses were conducted varying the time and temperature conditions to select the process parameters that led to the best compromise between yield, fluorescence emission, and degree of carbonization.

The goal was to combine the anti-inflammatory properties of garlic with the optical characteristics of nanoparticles to create carbon dots capable of acting as radical scavengers. Cellular viability studies were conducted using the proliferation assay (MTT assay) to assess the metabolic activity of A549-GFP cells exposed to carbon dots. The produced nanoparticles were characterized for fluorescence using a fluorimeter and UV-Vis Spectrophotometry. Their chemical composition was analyzed through Thermogravimetric analysis (TGA) and Fourier-transform Infrared Spectroscopy (FT-IR). Regarding nanoparticle size, measurements were performed using Transmission Electron Microscopy (TEM) and Atomic Force Microscopy (AFM).

1 Introduction

1.1 Classification of nanoparticles

Among the various nanoparticles, a distinction can be made between inorganic (i.e. quantum dots, gold/silver nanoparticles, iron oxide nanoparticles) and organic ones (i. e. liposomes, dendrimers, micelles, carbon dots, emulsions).

Inorganic nanoparticles encompass metallic [1], ceramic [2], and semiconductive particles [3], composed of materials distinct from carbon or organic substances. Metallic nanoparticles, derived from metallic precursors, exhibit a versatile range of structures including monometallic, bimetallic (formed as alloys or featuring a core-shell structure with distinct layers) [4, 5], or polymetallic configurations [4, 6]. These particles show unique optical and electrical properties, attributed to surface plasmon resonance (SPR) [4, 7]. Additionally, metallic nanoparticles exhibit thermal, magnetic, and biological characteristics, underscoring their considerable potential for applications in the realm of nanomedicine. Metal and metal oxide nanoparticles have been a focal point of extensive research owing to their diverse potential applications. Notably, AuNPs [8], renowned for their surface plasmon resonance, have found wide-ranging utility as biosensors. The exploration of magnetic nanoparticles has been directed toward medical applications, particularly in hyperthermic oncology [9, 10]. Within this realm of promising applications, the crucial consideration of biocompatibility and potential toxicity of nano-sized materials has attracted considerable attention [9, 11].

A study by Karlsson et al. [12] revealed an intriguing aspect regarding the cytotoxicity of metal oxide particles: their toxicity exhibited an upward trend as their size decreased from the micro to the nano level [9, 12]. This observation prompts a critical exploration of the impact of particle size, particularly as certain particles, when reaching the micro/nanoscale, retain a level of toxicity in vitro, despite being regarded as biocompatible at the macro level.

An advantage of inorganic materials is their high activity. Colloidal silver oxide [13], for instance, is extremely reactive and can kill various pathogens. However, the behavior of these materials *in vivo* differs from their behavior *in vitro*. For example, while silver oxide has a lethal effect on different cell lines in vitro, its efficacy and safety in vivo require a more in-depth evaluation [14].

The administration of inorganic materials presents specific challenges. Direct ingestion is impractical as inorganic materials can dissolve in the stomach. Sublingual administration may be an interesting alternative, as the material can be absorbed through the highly vascularized soft tissues under the tongue [15, 16]

In the bloodstream, nanoparticles may precipitate due to the concentration of water, salts, cells, and proteins. Therefore, intravenous, or topical administration is preferable to ensure that the material reaches its target. In the case of systemic administration, it is necessary to incorporate nanoparticles into

micelles to transport them through the bloodstream and reach the target cells. However, engineering the micelles is essential to ensure the appropriate release of the material into the target tissues [15, 16]..

Another issue is the excretion of nanoparticles. While some nanoparticles, like zinc, can be managed by the organism without significant issues, others may pose stress to the system. Therefore, it is important to consider not only the therapeutic efficacy of nanoparticles but also their safety and the organism's ability to manage and safely eliminate them.

Organic nanoparticles are composed of proteins [17, 18], carbohydrates [18, 19], lipids [20], polymers [21], or other organic compounds [22]. Dendrimers [23], liposomes [24], micelles [25], emulsions [26], nanogels [27], and protein complexes like ferritin [28] are among the most notable examples in this class. Generally, these NPs exhibit characteristics of being non-toxic, biodegradable, and, in certain instances, having a hollow core, as seen in the case of liposomes. Organic NPs are responsive to thermal and electromagnetic radiation, such as heat and light [29]. Additionally, they are often formed through non-covalent intermolecular interactions, rendering them more susceptible to changes in nature and providing a mechanism for efficient clearance from the body [10]. Organic nanoparticles are more straightforward to use as they are water-soluble. They can be administered through injection [30], oral ingestion [31], or aerosol [32]. However, it is crucial to make these particles selective for in vivo targeting. Unlike inorganic nanoparticles, which can be incorporated into liposomes, organic particles often utilize a prodrug. In practice, a peptide is attached to the nanoparticle, capable of recognizing a membrane receptor on a cell. When the nanoparticle reaches the cell, it is engulfed through receptor-mediated endocytosis. Inside the cell, it performs its function and, being polyester, is subsequently hydrolyzed by macrophages. After the cell's death, the nanoparticles are fragmented into small organic molecules easily absorbed by metabolism [33].

Some organic particles, such as those based on graphitized carbon, may pose disposal issues as the organism does not know how to handle them and considers them like inorganic nanoparticles [34]. It is essential for organic particles not to hydrolyze excessively before reaching the target [34].

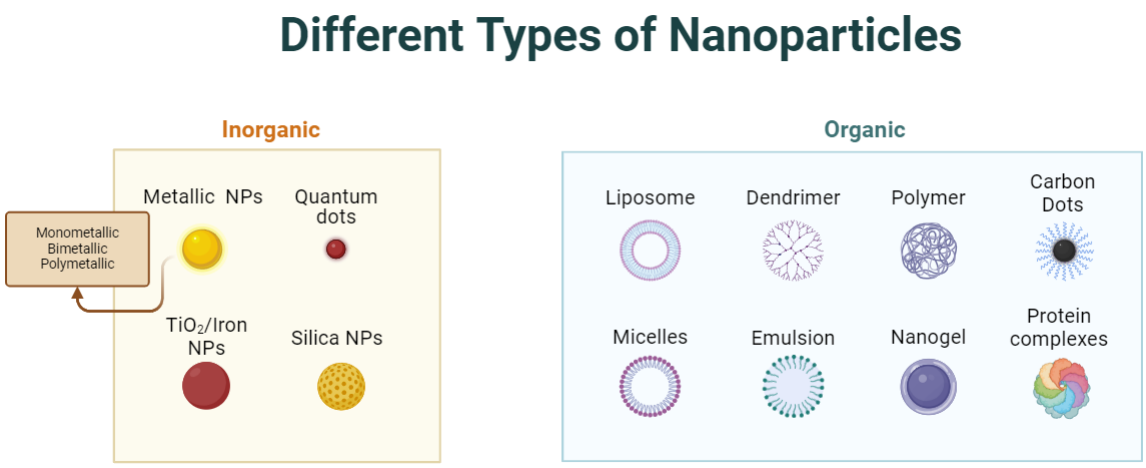

Figure 1: Different types of Nanoparticles.

1.2 Carbon dots

Carbon dots (CDs) are small and spherical nanoparticles, categorized as quasi-0D carbon-based materials [35]. They consist of a sp^2/sp^3 carbon skeleton which can exhibit a graphite lattice or amorphous carbon structure depending on the degree of carbonization of the CDs [36]. They feature various functional groups on their surface, such as carboxylic, hydroxyl, and amine groups, making them water-soluble and easily modifiable with the addition of organic or polymeric molecules [36]. Low toxicity, tunable optical properties, high photoluminescence quantum yield (QY), and accessibility through abundant low-cost sources made them available for a lot of applications. For instance, in biomedical fields, they are employed as drug and gene carriers, antimicrobial and antioxidant agents, bioimaging and theranostic particles. They are also used for photocatalysis, optoelectronics and biosensing [35, 37].

CDs were isolated for the first time in 2004 by Xu et al. [38] by chance. While purifying single-walled carbon nanotubes via gel electrophoresis, they obtained two impurities: the fluorescent carbon particles and the short tubular carbon. In 2006, Sun et al. [39] called the fluorescent one nanoscale carbon particles, that is carbon dots, to distinguish them from other carbon nanoparticles [40].

Thanks to several studies, it has been understood that varying the synthesis parameters, the optical and electrochemical proprieties of the resulting CDs change [40].

In this thesis activity, carbon dots are employed as antioxidants due to their scavenging capability. The study delves into the antioxidant attributes of CDs by exploiting their capacity to generate and absorb reactive oxygen species (ROS). This characteristic allows carbon dots to exhibit both free radical scavenging and antibacterial properties. These features represent two complementary aspects, as, while C0Ds act as antioxidants, they can also promote ROS formation. To assess their applicability in biological systems, cell cytocompatibility tests are conducted.

1.2.1 Classification

Due to the scientific community definition, classifying CDs poses challenges. Researchers named ‘carbon dots’ a diverse set of nanoparticles exhibiting a high-yield photoluminescence and nanometric size [37, 41], but this includes several compounds [37, 41]. So, this brings to problems of classification.

They can be classified by their synthesis method, or by their structure, or even by their properties and characteristics.

A first classification taxonomy of CDs can be made distinguishing between a top-down approach and a bottom-up one.

With a top-down method, the carbon dots are obtained from a bulky carbon-based material, i.e. carbon nanotubes, graphite, and graphene oxide, that is transformed into a blend of substances using different sources of energy [6]. Then they were purified and isolated by different methods, like dialysis and chromatography. [1]

In the top-down method, CDs are obtained from an initial carbon precursor through material fragmentation, resulting in nanoscale particles [42]. Conversely, in bottom-up synthesis, nanoscale materials are produced from small molecules or polymer precursors resulting in nanoscale particles, [36]. This approach is characterized by its ease of execution and cost-effectiveness.

An alternative classification method is based on the structure, specifically focusing on the core and shell regions of the nanoparticles. The "core" refers to the bulk of the material, representing the central portion of the nanoparticle, while the "shell" is the outer layer of the carbon dots.

There are various types of CDs, characterized by a graphitic core and an outer shell consisting of various functional groups, that can be categorized in graphene quantum dots (GQDs), carbon quantum dots (CQDs), carbon nanodots (CNDs), and carbon polymeric dots (CPDs) [36]. GQDs typically exhibit circular or elliptical shapes and consist of interconnected graphene oxide layers. The primary distinction between GQDs and CNDs lies in their synthesis methods. GQDs involve the carbonization of precursors, while CNDs are produced using alternative techniques. However, this differentiation based solely on synthesis methodologies may not be the most effective. To address this, carbon nitride quantum dots (CQNDs) have been introduced, featuring nitrogen-doped graphene layers that form a multilayer structure of C_3N_3 [37]. Given the similarity between GQDs and heteroatom-doped carbon nanodots (CQNDs), it has been proposed to group all GQDs with heteroatoms as xGQDs, where x stands for N, O, B, S, Si, etc. There are still few studies compared to those available for CDs [37, 43].

Contrarily, CPDs lack a graphene-like structure and form a diverse group with varying structures. As an alternative, classification based on chemical properties such as fluorescence emission wavelength, surface functionalities, and interaction with biomolecules or metal frameworks and nanostructures can

be considered. It is important to note that these three classification types may overlap, introducing the possibility of ambiguity [37].

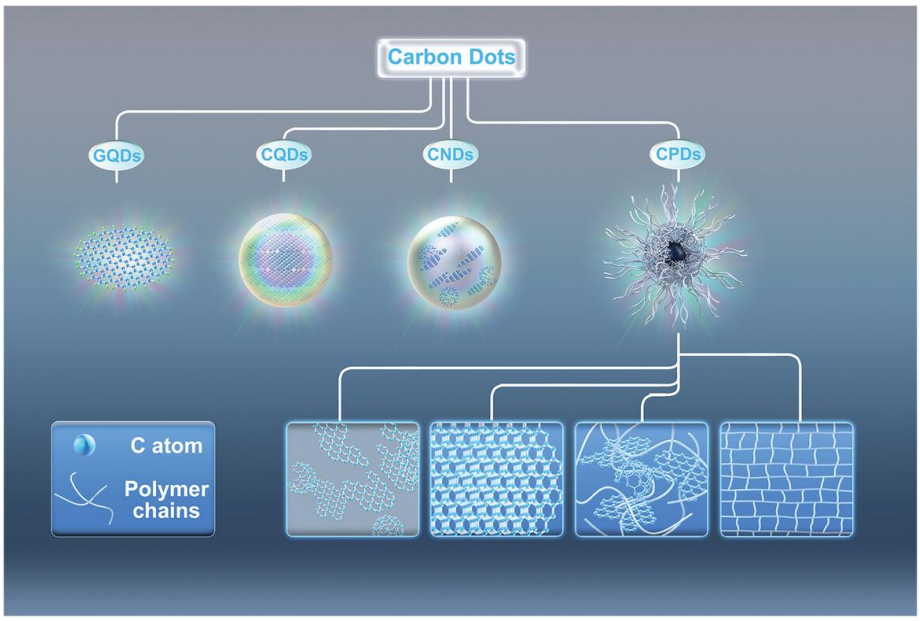

Figure 2: Classifications of CQDs as reported by Hia et al. [41]. Picture reprint under Creative Commons Attribution License 4.0 (CC BY).

1.2.2 Properties

One of the most interesting features of CDs is their strong and tunable photoluminescence. Numerous studies have been conducted to understanding the mechanisms driving the optical properties and fluorescence emission of carbon dots. Four main factors have been identified: the quantum confinement effect, surface states, molecular states, and element doping [44, 45].

The quantum confinement effect is a multifaceted phenomenon that governs their electronic, optical, and charge transport properties. The size and shape of the particles influence the electron motion. When the size of CDs is smaller than the Bohr radius of the exciton, electrons, and holes are confined within the nanoscale structure, resulting in a discrete energy level. As the size decreases, the energy levels become closer. This phenomenon results in a tunable bandgap, allowing to control of the absorption and emission wavelengths [46].

Energy-level transitions involve the movement of electrons between different energy levels within the CDs structure. It is intimately tied to their bandgap, which is the energy difference between the highest occupied molecular orbital (HOMO) and the lowest unoccupied molecular orbital (LUMO). The bandgap dictates the absorption and emission characteristics of CDs.

When CDs are excited by external energy sources, such as UV light, the confined electrons absorb energy and transit to higher energy levels. Upon returning to their original state, these electrons emit light, producing a fluorescence signal. CDs are mostly composed of graphitic sp^2-core, which is an aromatic domain, surrounded by a sp^3-carbon matrix which possesses a variety of functional groups.

When CDs have large π-conjugate domains in their core and few functional groups on the surface, the quantum confinement effect becomes pronounced, leading to distinct optical characteristics. As the size of the π-conjugated domain increases, a redshift in fluorescence emission is observed. In contrast, a blueshift in fluorescence emission is obtained with a decrease in sp^2 domains of the core and an increase in surface functional groups [44, 45].

CDs exhibit two fluorescence emission centers, one associated with the core and the other with the shell of the nanoparticle [47]. It is believed that the carbonaceous core is the primary cause of luminescence in aqueous CDs. Although numerous studies have highlighted the quenching properties of π-conjugated domains when CDs are in a solid state, such as aggregates [44, 48].

The surface states act as emissive center, influencing the radiative decay processes and determining the optical response of the CDs.

Surface state emission describes the emission of photons resulting from transitions associated with the surface states of CDs. These surface states are linked to functional groups that are on the surface of CDs, including hydroxyl, carboxyl, or amino groups. The emission of photons is influenced by the interactions between these surface states and the carbon core. These interactions create localized energy states on the surface, distinct from the bulk energy states within the carbon core. The surface states act as traps for charge carriers, and the recombination of these carriers results in the emission of photons, contributing to the overall photoluminescence of CDs.

The surface state emission mechanism is closely tied to the passivation of surface defects. Functional groups on the surface of CDs act as passivating agents, reducing the density of surface defects and trapping states. This passivation enhances the radiative recombination pathways, leading to the emission of light. Consequently, surface state emission serves as a distinctive feature that distinguishes CDs from other carbon-based materials.

The chemical groups found on the surface of the CDs constitute a single emission center. Some act as fluorescence activators, others as quenchers. The various functional groups have different energy levels, which may be related to their ability to supply electrons. The more electrons they can provide, the more energy they can generate.

Given the multifaceted and intricate nature of surface defect states, fluorescence emanating from these states exhibits pleochroism and luminescence dependent on the excitation source. Surface defects primarily arise from processes like surface oxidation, functioning as capture centers for excitons. Consequently, this interaction leads to the emergence of fluorescence attributed to surface defect states [45].

Research indicates that the photoluminescence behavior of CDs typically exhibits a dependence on excitation, although a minority of studies have documented excitation-independent emissions from these

particles. The wavelength-dependent emission is explained by the existence of distinct surface states. According to Tang et al., the blue emission (with an energy of 3.01 eV) is attributed to surface states such as C-OH, C=O, C-O-C, COOH, and others [49].

The molecular states arise from the carbon-based composition of CDs: the carbon core in CDs often consists of conjugated π-electron systems, where electrons are delocalized over adjacent carbon atoms. The presence of organic fluorophores made up of small molecules of carbonization contributes to the establishment of the fluorescent center [45].

In CDs, the conjugated carbon backbone allows for π-π* transitions, where electrons move from the highest occupied π orbital (HOMO-π) to the lowest unoccupied π* orbital (LUMO-π*). These transitions are responsible for the absorption of photons.

CDs, when doped with heteroatoms like nitrogen or sulfur, introduce additional energy levels that give rise to n-π* transitions. These transitions involve the movement of electrons from non-bonding orbitals (n) to the π* orbitals, contributing to the overall optical behavior of CDs. CDs doped with N and S exhibit excitation-independent emission, as observed by Yu et al., who synthesized three types of doped carbon dots: O-doped, N-doped, and N, S-doped carbon dots. The O-doped carbon dots display excitation-dependent emission and a low luminescence quantum yield (QY) [44], representing the ratio of emitted to absorbed photons [45]. This behavior is attributed to various surface trap states related to oxygen. Nitrogen doping introduces new surface traps with radiative recombination pathways. Upon the addition of sulfur, O-related states are removed, and N-related states are increased.

Through average lifetime measurements, they determined that the presence of N and S heteroatoms eliminates non-radiative relaxation pathways associated with O-related surface trap states. This leads to an excitation-independent mechanism of fluorescence, as evidenced by their findings [44].

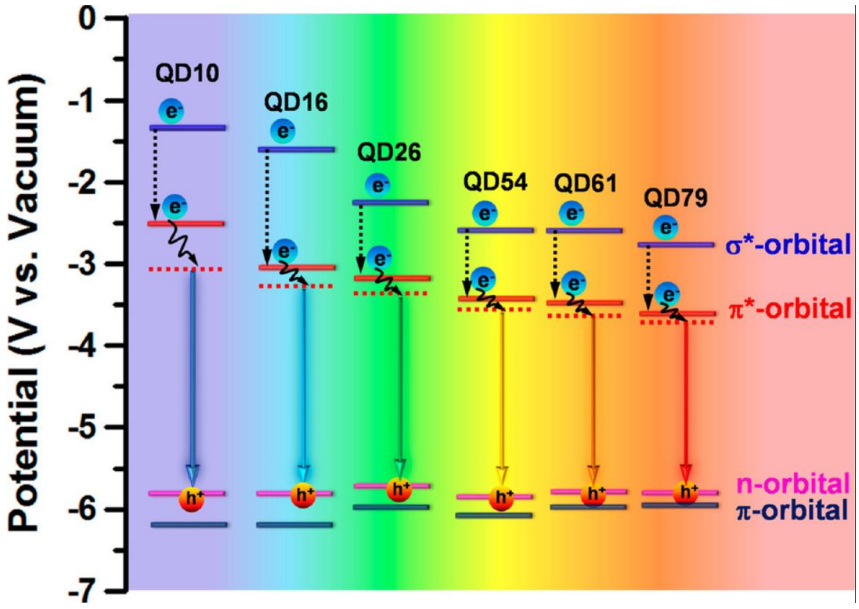

Figure 3: Schematic energy level diagram associated with size-dependent PL emissions from the GOQDs. Reprinted with permission from [49]. Copyright © 2016 American Chemical Society.

Based on findings from steady-state spectroscopic investigations, it is asserted that the photoluminescence in carbon dots containing oxygen originates from defect states associated with vacancies, interstitial atoms, and diverse functional groups. In contrast, for CDs lacking oxygen, the predominant source of photoluminescence is the intrinsic conjugated core, primarily attributed to the quantum confinement effect.

By altering the molar ratio of the precursors, regulating the reaction temperature, and varying the size of the conjugated π-domains, it is possible to modulate the color emission of CDs.

The optical properties of carbon dots are intricately tied to their structure. Graphene quantum dots GQDs are nearly spherical anisotropic particles with a height of approximately 2 nm and a width of less than 20 nm. They feature a core composed of graphene sheets that host chemically arranged groups between the layers. Due to their dimensions and the presence of non-interacting π-conjugated domains with defects between graphene planes, the primary fluorescence emission is attributed to the quantum confinement effect. The presence of oxygen atoms increases the number of emission centers associated with π-conjugated domains [36].

CQDs exhibit a graphene core surrounded by a shell containing various functional groups. The emission of these nanoparticles can be modified by altering their size [36].

The CNDs exhibit a pronounced carbonization degree coupled with surface chemical groups. However, they typically lack discernible crystal lattice structures and polymer characteristics. The primary source of photoluminescence is attributed to the defect/surface states and subdomain states within the graphitic carbon core, with the absence of the quantum confinement effect associated with particle size [36].

Possessing a hybrid polymer/carbon structure, CPDs feature abundant functional groups and polymer chains on the surface enveloping a carbon core. This carbon core can be categorized into four subclasses, including two with fully carbonized cores like CNDs or CQDs, a paracrystalline carbon structure comprising small carbon clusters surrounded by polymer frames, and a densely crosslinked and dehydrated polymer frame structure. In the context of CPDs, the origin of photoluminescence predominantly arises from surface states, subdomain states, and molecular states.

1.2.3 Structure

The structure of CDs is strictly connected with the features of these nanoparticles. It is distinguished between GQDs, CQDs, CNDs and CPDs.

GQDs typically comprise a few layers of an oxygenated graphene-like arrangement, wherein highly oxidized functional groups, notably carbonyls and carboxylic entities, are concentrated predominantly at the edges. These GQD layers exhibit, according to the Lerf– Klinowsky model for graphite oxide, a discernible classification into four distinct types, which are triangular, rectangular, hexagonal, and dendrimeric (Types 1–4), as systematically outlined in prior literature [50], with consequential impacts on the HOMO–LUMO gap [51].

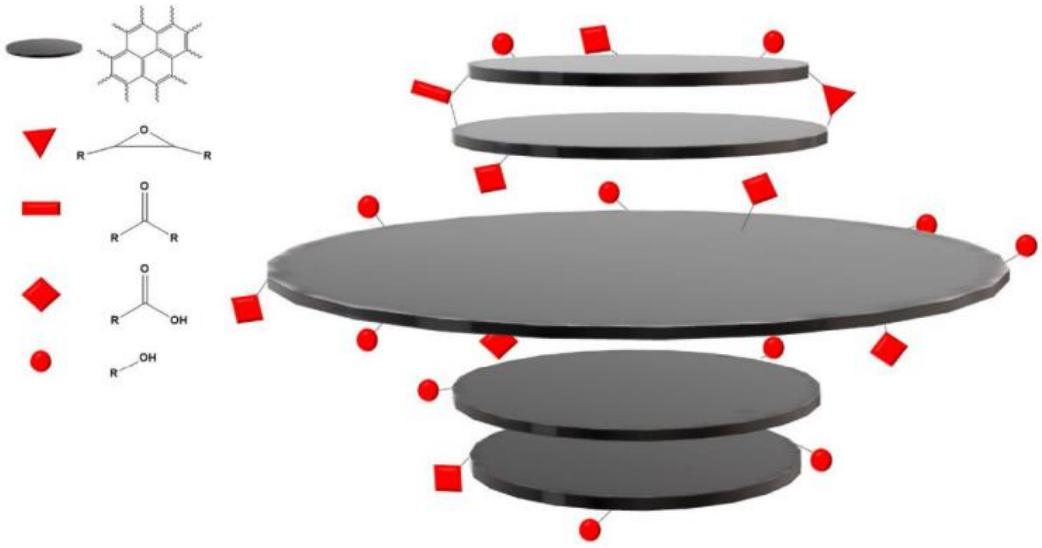

Figure 4: Schematic structure of GQDs. Reprinted with permission from Mintz et al.[52] .

Furthermore, GQDs demonstrate a noticeable solubility profile [53], or, at the very least, they can be dispersed in water to form colloidal suspensions [54].

CQDs are rounded nanoparticles with crystal lattices embedded in the core, with various functional groups on the surface [55]. CNDs are delineated as small, carbonized nanoparticles devoid of well-defined crystal lattices within the core yet presenting select functional groups on the surface [56].

The intrinsic versatility of GQDs is underscored by their ease of functionalization through the incorporation of heteroatoms. These heteroatoms may be introduced post-synthesis as doping agents [57] or integrated into the graphene-like structure during GQD production, as in the case of CQNDs synthesis [58].

CQNDs attract significant attention due to the integration of nitrogen atoms within the graphene-like layers, imparting unique and distinctive properties to these nanostructures.

As documented by Liyanage et al. [59], the CQNDs are derived through the substitution of oxygen atoms in GQDs with nitrogen atoms, introducing a structural complexity that surpasses initial expectations. Indeed, there is a modification in the core structure, resembling that of materials constituted by layers of C_3N_3.

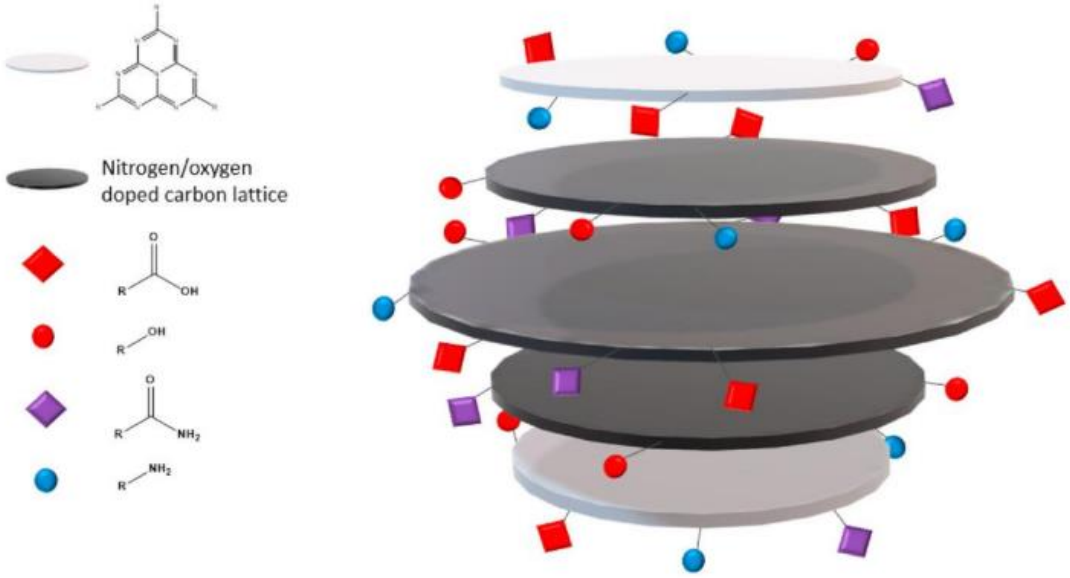

Figure 5: Schematic representation of CQNDs. Reprinted with permission from Mintz et al. [52]

Employing highly reactive precursors facilitates the generation of heptazine layers on the terminal segments of CDs. Kirbas and co-authors [60] noted that variations in the origin of the utilized precursors do not result in substantial morphological changes, but rather induce modifications in the terminal groups of the particles. Furthermore, Wiśniewski et al. [61], underscored the importance of functionalized terminal segments of CDs in their interaction with water, as evidenced by the formation of [OH(H2O)n] clusters through a proteolytic process.

CPDs have complex and heterogeneous structures, lacking the graphene structure and they can be categorized into two primary groups: one comprises CDs resulting from polymer degradation, and the other encompasses PCDs formed through the condensation of molecular units. The first group is characterized by the partial retention of the polymer's original structure and functionalities [62]. However, investigations into these PCDs have been limited, primarily focusing on surface residue

composition. In contrast, PCDs synthesized from molecular precursors offer enhanced ease of characterization through the modeling of their reactivity.

1.2.4 Synthesis Methods

Over the years, the synthesis of carbon dots has undergone a lot of changes, and it now includes a variety of methods that differ according to their simplicity, scalability, and properties of the resulting nanoparticles.

The methodologies employed for the synthesis of CDs can be divided into two primary approaches: the top-down and bottom-up strategies.

The top-down approach encompasses the generation of CDs derived from the disruption of larger carbon-containing materials. Techniques belonging to this methodology comprise arc discharge, laser ablation, electrochemical synthesis, nanometer etching, as well as hydrothermal, solvothermal, and severe oxidation methods [63].

The use of laser ablation involves the utilization of a high-energy laser to irradiate the material, which leads to quick heating. The sample is knocked off by small craters created by pulsing the lasers leading to the consumption of the materials and generation of plasma that flows on the sample surface, thus ionizing it. The technique allows for careful control over size distribution, and CDs thereby formed can have high crystallinity. However, this method could be equipment-intensive and not easily scalable for large-scale production.

In arc discharge synthesis [63, 64], the process initiates with the creation of an electric arc between two carbon electrodes in an inert gas atmosphere, typically helium or argon. The high temperature generated during this arc discharges vaporizes and ablates carbon from the electrode surface. The vaporized carbon species then undergo rapid cooling and condensation, leading to the formation of CDs.

It is important to highlight that although CDs generated using this method demonstrate notable fluorescence, there is a notable drawback. The particle size distribution tends to be inconsistent, and the yield is exceptionally low, rendering it unsuitable for large-scale manufacturing.

The process is also characterized by high energy consumption, with the generation of an electric arc demanding a substantial amount of energy. This not only contributes to elevated production costs but also raises environmental concerns related to energy efficiency.

The oxidation method represents a synthesis strategy for CDs that involves oxidizing and decomposing large-sized carbon sources into small carbon nanomaterials. This approach can be categorized based on the oxidant used, with distinctions between chemical oxidation and electrochemical oxidation methods.

In the chemical oxidation process [65], robust oxidants are employed to break the covalent bonds within the carbon source, gradually transforming it into smaller molecules. The progression of the reaction is

closely tied to the oxidizability of the oxidant. The size, structure, and properties of the CDs synthesized through chemical oxidation are predominantly influenced by the choice of oxidant and the oxidation process. In contrast, the properties of the final product are minimally affected by the source of the reaction substrate.

Electrochemical oxidation [66, 67] involves utilizing a potent oxidation potential to induce oxidative stripping of the carbon source on the electrode, leading to the formation of CDs. This process bears similarity to the principle of arc discharge and contributes to the controlled synthesis of CDs through electrochemical means. This method offers advantages such as ease of operation, high yield, and controllable conditions. However, it necessitates specialized equipment and faces limitations concerning suitable precursors.

Pyrolysis [68] involves the carbonization of organic precursors at elevated temperatures in an inert atmosphere, leading to the formation of carbon dots with the gradual transformation of the organic matter through processes involving heating, dehydration, degradation, and carbonization. It allows to production of highly crystalline carbon dots with well-defined properties. The process may require careful control of temperature and reaction time to achieve desired results. The pyrolysis method is characterized by its straightforward operation, and it offers diverse heat generation options. For instance, microwave-assisted pyrolysis simplifies the application of the pyrolysis method, making it widely applicable.

Nanometer etching [69] involves the use of specialized techniques to create nanoscale features on a larger carbon structure. This process allows for the controlled disintegration of the carbon material, resulting in the production of CDs with specific characteristics.

Bottom-up synthesis [70] involves the assembly or growth of smaller molecular precursors into larger entities, ultimately forming the desired CDs. The process typically begins with the selection of suitable precursor molecules, which can range from organic compounds to heteroatom-containing molecules. Through controlled chemical reactions or self-assembly processes, these precursors undergo transformation into CDs, offering a high degree of control over size, structure, and surface functionalities. Among the various techniques there is the microwave-assisted method, template method, and hydrothermal/solvothermal method synthesis.

The microwave-assisted method [57, 71] enables the carbonization of a precursor in a solution at high temperatures through microwave irradiation, allowing for the rapid mass production of CDs within ten minutes. Owing to its efficiency, simple operation and equipment demand, the microwave method is an effective technique with significant potential for the large-scale production of fluorescent CDs.

The hydrothermal/solvothermal method [56, 72, 73]entails a synthesis technique where the reaction mixture interacts with water or an organic solvent within a sealed system, such as an autoclave, under specific temperature and autogenous pressure conditions. The distinction between hydrothermal and

solvothermal lies in the type of solvent employed. This method is widely adopted for its simplicity, safety, and efficacy. Moreover, the raw materials for hydrothermal reactions are abundant, facilitating easy scalability. Notably, it promotes economic and environmentally friendly production practices, with straightforward post-treatment processes.

Solvothermal synthesis [68, 74], a commonly utilized variant, offers excellent controllability. By adjusting the reaction substrate, temperature, and duration, significant alterations in product properties can be achieved. It is pertinent to note that solvothermal substrates are not limited to small molecules; biomass macromolecules are also viable candidates. The extraction of CDs from biomass resembles a cooking process, where high temperatures and pressures break down macromolecules, dissolving them into a solution like a "CDs soup."[63] The inherent diversity of biomass translates to CDs with rich properties, while the abundance and variety of biomass sources facilitate large-scale synthesis.

However, the synthesis of CDs from biomass follows a somewhat trial-and-error approach, lacking the directed synthesis of functional CDs. This blind synthesis process may impede the precise control over CDs' properties, limiting their tailored functionalities.

Due to all these advantages, in this thesis work, a hydrothermal synthesis has been employed to produce garlic CDs, using garlic as the starting biomass.

1.2.5 Biomedical applications

In recent years, carbon dots have emerged as a promising class of nanomaterials with a wide range of biomedical applications. These fluorescent nanoparticles, typically sized below 10 nanometers, exhibit unique properties that make them highly suitable for various biomedical purposes, like bioimaging, biosensing, drug and gene delivery, diagnostic and theranostic activities, antimicrobial applications and antioxidant agents.

Their remarkable optical features, characterized by robust fluorescence and photostability, position them as optimal choices for biomedical imaging. Their compact size, adjustable fluorescence, and minimal cytotoxicity further amplify their usefulness in cellular imaging, fluorescence microscopy, and in vivo imaging. Modulating their luminescence allows them to penetrate different tissues [75]: emitting in blue, they can reach the dermis; in green, they can penetrate down to adipose cells beneath the dermis, up to a depth of 3 mm; in red, they can reach a depth of 5 mm; while in the near infrared (NIR), they can penetrate muscles. This enables cellular imaging without the need to genetically modify cells to make them fluorescent.

Moreover, the capacity to functionalize carbon dots with precise targeting ligands enhances their effectiveness in targeted imaging, particularly for the early detection of diseases.

Their exceptional optical properties make them ideal for bioimaging, as they emit fluorescence when excited at a specific wavelength.

CDs present promising prospects as candidates for chemical and fluorescence sensing. The interplay between metal ions and the surface functional groups of CQDs instigates the creation of new electron-hole recombination, inducing a shift in the fluorescent characteristics of CDs via energy transfer pathways [41, 76]. This capability positions CDs to serve as fluorescence sensors for detecting heavy metal ions in aqueous solutions or living cells. In a standard experimental setup, Zhou et al, show the efficacy of unmodified CQDs as fluorescence-sensing agents for the detection of highly toxic metal ions, specifically Hg^{2+}, and thiols, like cysteine, homocysteine, and glutathione [41, 77]. Their findings revealed that Hg^{2+} could quench the fluorescence of CQDs, while biothiols played a crucial role in efficiently preventing fluorescence quenching by removing Hg^{2+} from the surface of CQDs [41, 77]. Furthermore, the versatility of CDs in chemical sensing extends to the detection of heavy metal ions such as Fe^{3+}, Cu^{2+}, Cr (VI), Ag^{+}, and Pb^{2+}, where the formation of fluorescent quenching proves the effectiveness of carbon dots as chemical probes.

Despite their potential as fluorescent probes for selective and sensitive detection of cellular ions, antibodies, proteins, and nucleic acids, uncertainties persist regarding the elimination route, degradation times, and detection limits with high sensitivity for clinical applications.

CDs demonstrate notable photocatalytic activity, decomposing various substances under light irradiation. Yet, challenges persist in understanding their degradation efficiency, recombination loss, and the effectiveness of interfacial charge transfer. Acting as photosensitizer agents, CDs can generate reactive oxygen species (ROS) to eliminate cancer cells under light exposure. However, there is limited knowledge regarding their efficacy in treating large, deeply hidden tumors and the optimal doses for clinical studies, as CDs are still in the preliminary stages of investigation. CDs also function as photothermal agents, displaying significant cytotoxicity against cancer cells when exposed to light. These agents possess strong light absorption characteristics, particularly in the NIR region, effectively converting light energy into hyperthermia. This localized heat generation enables the targeted destruction of cancer cells, minimizing adverse effects on normal cells [9, 41, 76, 78, 79].

Numerous studies affirm the applicability of CQDs in photothermal therapy (PTT) for cancer treatment. For instance, Ge et al. [41, 80] explored the utilization of CQDs derived from polythiophene phenyl propionic acid in PTT. Their findings revealed significant cytotoxicity of the prepared CQDs against HeLa cells upon exposure to a NIR laser. Moreover, the demonstrated high in vivo PTT efficacy of CQDs in tumor-bearing mice, coupled with minimal toxicity, underscores the potential of CQDs in the realms of cancer diagnosis, treatment, and bioimaging in living mice [41, 80].

The ability of CDs to generate radicals and reactive oxygen species makes them immediately applicable in photodynamic therapy [81, 82]. It has become evident that, beyond exhibiting oxidant properties

under illumination, CDs can function as radical scavengers and antioxidants. The potential of CDs to serve as nanozymes has been rapidly recognized. The unique capacity for both oxidation and antioxidation is uncommon [81, 83], presenting another significant challenge posed by CDs.

Nonetheless, there is a lack of understanding regarding the effectiveness of deeper tissue heating and thermotolerance in clinical studies, as CDs remain in the preliminary stages of research. In terms of tracking and delivering genes or drugs to specific targets, CDs exhibit effectiveness [41]. Indeed, CDs play a pivotal role in regulating drug release. Loading CDs with doxorubicin has been shown to modulate drug release in HeLa cells [29, 41, 84-86]. However, gaps persist in understanding their specificity for targeting certain disease states [41].

1.3 Cytocompatibility of carbon dots

The inherent non-toxic and environmentally friendly nature of carbon makes the carbon cores of CDs non-toxic as well. It has been established that cytotoxicity primarily arises from the passivating agent on the surface of CDs. Therefore, the use of surface passivating chemicals with low toxicity allows *in vivo* imaging at high concentrations [41].

In vitro investigations conducted by Ding et al. [41, 87] have elucidated that DNA-CQDs, derived from bacterial DNA, undergo internalization by human embryonic kidney cell lines (HEK 293). The inherent fluorescence of DNA-CDs facilitates imaging using a confocal microscope, thereby highlighting the utility of DNA-CDs as luminescent probes for cell imaging studies [41, 87]. In a separate study by Zheng's research group, it was demonstrated that CQDs exhibit exceptional biocompatibility and possess highly tunable photoluminescence properties. Moreover, these CQDs can traverse the blood–brain barrier with ease, selectively targeting C6 glioma cells without the necessity for additional targeting molecules [41, 88]. Singh and colleagues conducted comprehensive *in vitro* and *in vivo* toxicity assessments of nitrogen-doped carbon quantum dots (NCQDs). In the standard in vitro experiment, the lactate dehydrogenase (LDH) profile, cell apoptosis, DNA fragmentation, and growth cycle of the HeLa cell line were examined following exposure to NCQDs [41, 89]. The findings indicated a notable absence of toxicity against these cancer cell lines.

In the in vivo toxicity study, Singh et al. [41, 89] administered two distinct concentrations of NCQDs to mice over a 30-day period. The evaluation encompassed antioxidant levels, serum biochemistry, hematological parameters, and histopathological analysis, revealing no discernible toxicity of CQDs at either concentration [41, 89]. Consequently, these results affirm the safety profile of CQDs, endorsing their application in the realm of nanomedicine. Recently, drug delivery systems (DDSs) depending on nanotechnology have been widely investigated. Unfortunately, various nanomaterials that can act as drug delivery vehicles, such as graphene oxides, mesoporous silica (MS), polymeric nanoparticles and gold nanoparticles (AuNPs), have toxicity and biocompatibility issues that limit their application in

clinical therapy [41, 84, 90]. The requirement of thiol groups for drug loading through the Au-Thiol interaction further limits their application in drug delivery because it reduces the choice of possible drugs to be chemically conjugated with the nanoparticles. [22, 41]. This has resulted in considerable attention of researchers in discovering more promising nanomaterials to replace AuNPs. As an emerging class of luminescent nanomaterials, CDs have shown potential as drug delivery agents, as they have demonstrated excellent biocompatibility properties, high water solubility and flexibility in surface modification with other chemical molecules [41, 84, 90]. For example, Zheng and colleagues conjugated oxidized oxaliplatin (Oxa(IV)-COOH), which is a type of platinum based anticancer pro-drug that is applied in the pharmacotherapy of metastatic colorectal cancer on the surface of CQDs by condensation response between the carboxyl group of Oxa(IV)-COOH and amino group on the CQDs' surface through chemical coupling [88].

1.3.1 Cytocompatibility and CDs internalization

For biomedical application, the biocompatibility of designed CDs and the lack of toxicity must be assessed. When evaluating cytocompatibility, it is necessary to consider the context in which they are used. Biocompatibility and toxicity can be assessed by:

- *In vitro* assays

- *In vivo* analysis

Unfortunately, promising results obtained during *in vitro* evaluation, may not be confirmed in animal models which resemble better the physiological condition of a specific tissues or human body.

Another aspect to consider is the choice of the biological model, i.e., the cell line used. The choice is based on the aspect to investigate, i.e. interaction with the immune system, killing of cancer cell lines [91], nanoparticles internalization and accumulation in different organelles [92]. This is reflected in

the choice of the type of experiment to be performed, the material to be used and the cell line to be tested.

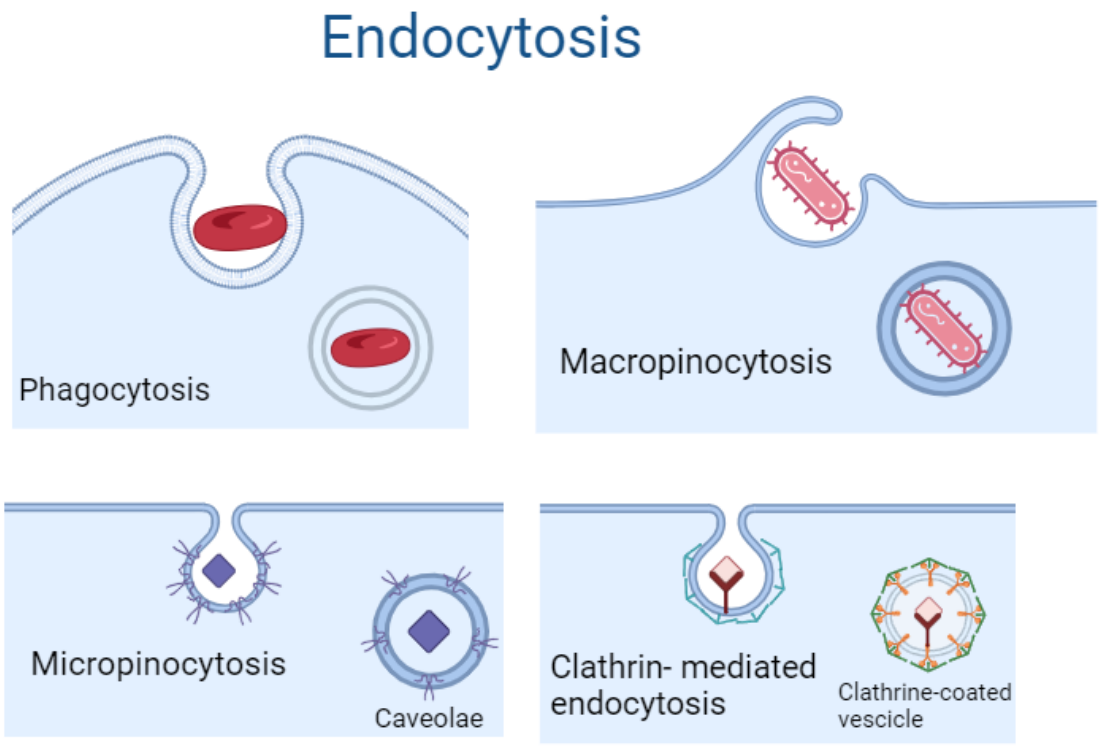

Figure 6: Different types of endocytosis.

Cellular membrane is a semi-permeable barrier that allows the selective passage of certain substances and molecules. Substances unable to permeate the membrane necessitate assistance from passive diffusion mechanisms (simple and facilitated diffusion), energy-dependent active transport, or endocytosis.

Endocytosis involves membrane invagination, resulting in vesicle formation and internalization of substances. There are three mechanisms of endocytosis, namely phagocytosis, pinocytosis, and receptor-mediated endocytosis. With phagocytosis particles larger than 250 nm in diameter are introduced into the cell., while pinocytosis mediates uptake of fluids and solutes. Pinocytosis occurs via micropinocytosis and macropinocytosis, forming small (0.1 micrometers in diameter) caveolae vesicles or larger (0.5 to 5 micrometers in diameter) vesicles, respectively.

Receptor-mediated endocytosis selectively internalizes specific molecules. Molecules bind to membrane receptors located in clathrin-coated pits before internalization. Clathrin-coated vesicles form upon receptor binding, fuse with early endosomes for sorting, and undergo subsequent removal of clathrin coating, releasing contents into the cell.

The internalization of CDs is a process influenced by various factors, primarily the cell type, exposure time, dose, surface charge, and particle size. The energy required for internalization plays a significant

role, with potential involvement of caveolae-mediated endocytosis, clathrin-mediated pathways, or diffusive transport [93].

It must be verified whether cellular internalization of the nanoparticles has occurred, whether the material enters the cell or not. If there is no internalization, it is important to evaluate whether there are still effects inducing cell death, such as chemical oxidation or photooxidation.

If the material enters the cell, it is crucial to investigate which cellular mechanism it interacts with. This may include oxidative stress, cell lysis due to hydrolysis, or disruption of cellular mechanisms such as protein synthesis, transcription, or translation, depending on the material.

The initial stage of nanoparticle interaction with cells is represented by the cell membrane. To assess the effect of nanoparticles on the membrane, in vitro studies employing liposomes are conducted. They can modulate membrane properties, allowing for straightforward data acquisition regarding structural and thermodynamic characteristics [94]. Mavrodi et al. [94], investigated the impact of N-doped CDs on the structural and thermodynamic properties of the phospholipid bilayer. They used dipalmitoyl phosphatidylcholine (DPPC) and negative charged dipalmitoyl phosphatidylglycerol (DPPG) with a low molar content (5%). To stabilize the membrane, a low molar content (5%) PEGylated phospholipid was added to replicate the negative charges of glycosamineglycan (GAGs) attached to cellular membranes.

The primary interaction occurs through electrostatic forces, specifically between the negative charge of the membrane and the slightly positive charge of the CDs, increasing CDs adhered to the bilayer surface. Solutions of CDs in PBS or water show slightly different outcomes, with less effective interaction in PBS compared to water. However, specific interactions between CDs and the membrane cannot be ruled out, as CDs were found to adhere to the model even under conditions of high ionic strength and temperature [94].

Through techniques such as zeta potential analysis, a slight increase in measured potential and associated charge on the membrane was observed. A change in membrane shape was noted, particularly an enlargement of the polar head of the outer phospholipid layer, causing a shift in liposomal membrane curvature. Among the proposed hypotheses to explain this phenomenon, osmolarity was ruled out, as it remained unchanged in the PBS solution. However, a variation in the size of counterions, in this case CDs, can modify membrane curvature. Thus, CDs, when interacting with the membrane, behave as counterions, altering membrane curvature and resulting in a reduction in liposome size.

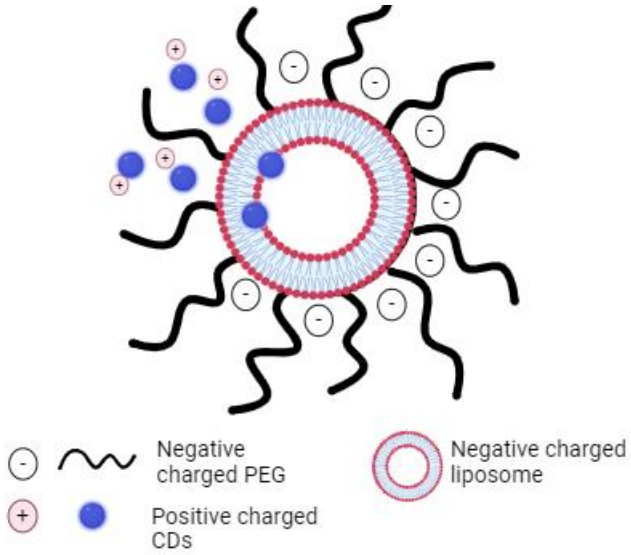

Figure 7: Electrostatic interaction between negatively charged PEGylated liposome and positively charged CDs.

Tests revealed a change in the reversibility of the liposomal dispersion dissolution reaction, where the presence of CDs led to a reduced reversibility of this transition. Additionally, an increased permeability of the phospholipid bilayer was observed, measured through the external release of DOX loaded in liposomes in the presence and absence of CDs. At higher concentrations (500 µg/mL), an "anomalous" transport is observed, stemming from both diffusion and relaxation-mediated release [93].

Once inside the cell, CDs distribute within endolysosomal structures, the Golgi apparatus, and, in some instances, even reach the nucleus through nuclear pores. Studies by Sun et al. [95], indicate that the internalization of CDs is temperature-dependent. Specifically, treating MCF-7 cells at 4 °C with PPEI-EI-passivated CDs resulted in marking both the cytoplasmic membrane and the cytoplasm, but not the nucleus. The influence of nanoparticle size has been observed by Ray et al. [96], demonstrating that 2-6 nm CDs subjected to acidic oxidation reach both the cytoplasm and the nucleus after a 30-minute incubation.

Additional insights into internalization come from Goh et al. [97], who noted that CDs with amino groups, carrying a positive charge, interact more efficiently with the cell membrane and are internalized through endocytosis. Liu et al [98] analysis of PEI-passivated CDs revealed their presence within endosomal structures after a 3-hour transfection [93].

Exploring internalization in neural cells, Zhou et al. [93] used PC-12 and RSC96 rat cells. Their results show that after 5 minutes, CDs are present in the cytoplasm without accumulation in the membrane. After 15 minutes, they are observed in the nuclei, while after 360 minutes, numerous particles are found in the cytoplasm and few in the nucleus. The hypothesis of a diffusive mechanism within the nucleus is suggested due to the smaller size of nuclear pores compared to CDs [93].

To further understand the internalization process, the FACS at 4 °C and specific inhibitors were employed. Experiments indicate a significant reduction in CD uptake at low temperatures, suggesting the involvement of both ATP-dependent and diffusive transport mechanisms. Additionally, the use of inhibitors for caveolae and clathrin-mediated pathways reduced CD uptake, while macropynocitosis inhibition showed no significant variations [93].

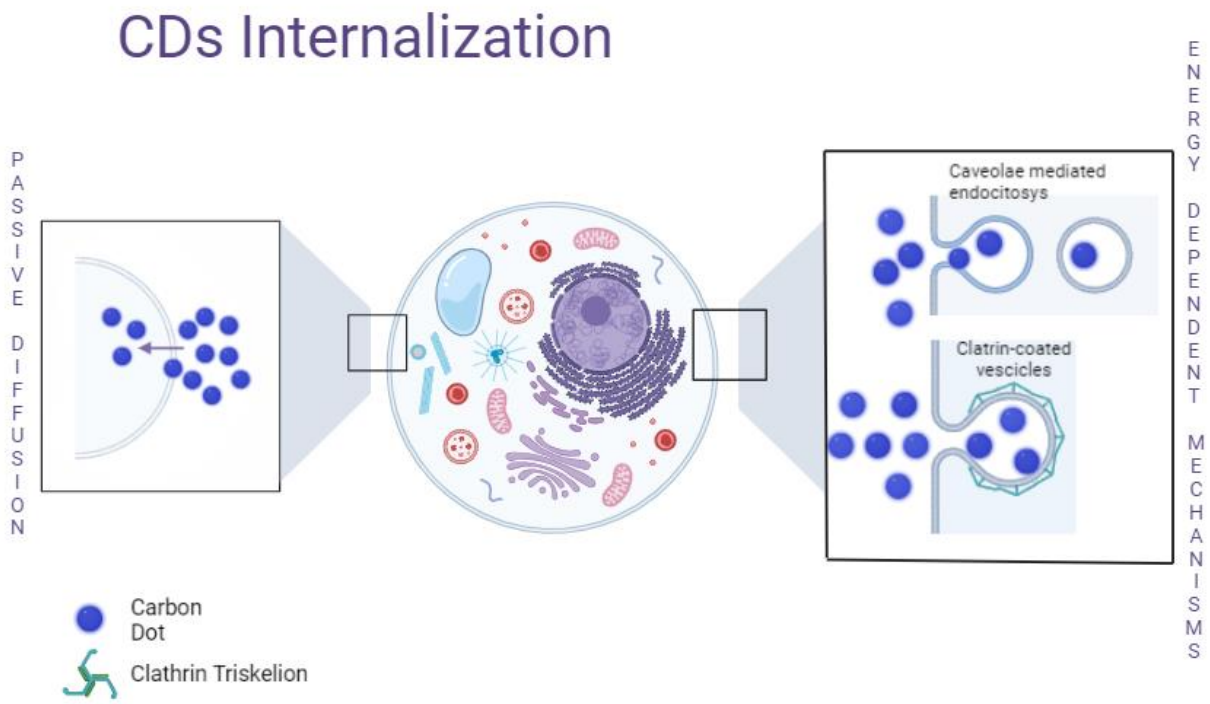

Figure 8: Mechanisms of CDs internalization.

Further investigations, including the use of organelle markers, revealed that CDs are initially directed toward lysosomes through the endocytic pathway, then reach the Golgi apparatus through retrograde trafficking pathways and the nucleus through diffusion via nuclear pores. The observation of CDs in limited quantities within mitochondria explains cytotoxicity, while their minimal presence in the endoplasmic reticulum has also been documented [93].

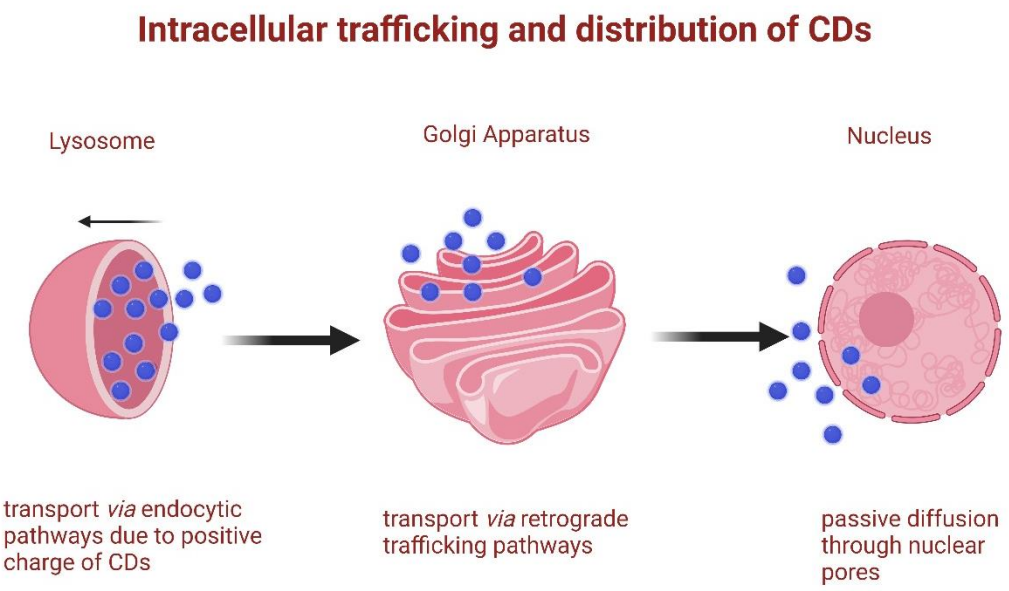

Figure 9: Intracellular trafficking and distribution of CDs.

1.4 Radical Scavenging effect

The term "radical scavenging" refers to the ability to mitigate oxidative stress induced by reactive oxygen species (ROS). In the human body, numerous ROS, including hydrogen peroxide, peroxyl radicals, hydroxyl radicals, superoxide anion radicals, hypochlorous acid, nitric oxide radicals, and singlet oxygen exist, and their concentration must be regulated to prevent cell death, lipid peroxidation, and damage to proteins and DNA [99]. Managing the levels of these reactive species is crucial for preserving cellular integrity and mitigating oxidative stress-related damage [100]. Although reactive oxygen species (ROS) can exert toxic effects on cells, the controlled generation of ROS can serve as an active tool for antibacterial, antiviral applications, or photodynamic therapy.

Certain carbon nanomaterials exhibit a notable dual response to reactive species: they can function as scavengers, reducing the number of free radicals and ROS, or they can generate reactive species under irradiation. This dual nature is absent in single-molecule antioxidants like ascorbic acid and is instead a distinctive and intriguing property of several carbon nanomaterials. Specifically, CDs can display both antioxidant and oxidant responses. However, these properties are closely correlated with the synthesis and processing pathway [81].

1.4.1 Garlic antioxidant properties

Allium represents the predominant vegetable genre within the Alliaceae family, comprising 700 species globally [101], with Allium sativum being the most widely cultivated and utilized in India and Pakistan for both culinary and medicinal purposes [102, 103]. Renowned for its nutritional richness, Allium sativum contains carbohydrates, minerals, antioxidants, vitamins, polyphenols, and carotenoids[104]. Notably, it serves as the richest source of sulphur-containing compounds, encompassing a variety such as an ajoene, allicin, alliin, allyl sulphides, allyl disulfides, allyl trisulfides, cysteine, cycloalliin, cysteine

sulfoxides, cystine, diallyl sulphides, dimethyl sulphides, glutathione, disulfides, methionine, methyl sulphides, sulfanes, pseudoscordinine, thiosulfates, scordinine, trisulfides, and tetrathiol [105, 106], along with essential minerals including phosphorus, calcium, iron, selenium, and germanium. This extensive composition makes Allium sativum a potential antioxidant, therapeutic, antibacterial, and anticarcinogenic agent [103, 107].

Garlic compounds have demonstrated modulating effects on oxidative stress by scavenging ROS, augmenting cellular antioxidant enzymes, and enhancing glutathione levels [108]. The potential applications of garlic extend to various health disorders, including inhibiting colon tumor development [109], addressing non-alcoholic steatohepatitis [110], mitigating murine colitis [111], inducing apoptosis in human gastric carcinoma cell lines [112], inducing cell cycle arrest in cancer cell lines [113], reducing blood pressure [114], and exhibiting anticancer properties [103].

1.4.2 ROS production

Oxygen, with a couple of unpaired electrons in the outer valence shell, forms reactive species. ROS can manifest as free radical oxygen intermediates such as hydroxyl radicals ($^{\bullet}OH$) and superoxide anions ($O_2^{\bullet-}$), or as non-free radicals like hydrogen peroxide (H_2O_2) and singlet oxygen ($^1O_2$) [81, 83].

The superoxide anion is generated through the reduction of molecular oxygen during the reaction:

$$O_2 + e^- \rightarrow O_2^{\bullet-} \quad \textbf{(1)}$$

Following this, it undergoes dismutation, yielding hydrogen peroxide and molecular oxygen as products:

$$2\ O_2^{\bullet-} + 2\ H^+ \rightarrow H_2O_2 + O_2 \quad \textbf{(2)}$$

Upon the partial reduction of hydrogen peroxide, there is the formation of hydroxide ions, hydroxyl radicals, or water, depending on the extent of the reduction:

$$H_2O_2 + e^- \rightarrow HO^- + {}^{\bullet}OH \quad \textbf{(3)}$$

$$2\ H^+ + 2\ e^- + H_2O_2 \rightarrow 2\ H_2O \quad \textbf{(4)}$$

$^1O_2$ is an intriguing species with powerful oxidizing capabilities, emerging when molecular oxygen becomes excited. Despite not being a radical, its behavior is notable in its ground state due to the presence of two distinct antibonding orbitals, labeled as π_x^* and π_y^*, each occupied by a single electron with the same spin. The various electronic states of molecular oxygen, including the excited singlet states $^1\Sigma g^+$ and $^1\Delta g$, as well as the ground triplet state $^3\Sigma g^-$, originate from the complex arrangement of its molecular structure.

A particularly fascinating aspect is the metastable singlet oxygen ($^1O_2(^1\Delta_g)$), characterized by a unique electron configuration where both electrons are paired in a single orbital. Despite its lower energy state, this singlet oxygen variant exhibits a significantly prolonged lifetime compared to the excited $^1\Sigma g^+$ state, adding to its distinctive properties.

In the singlet excited state, the spin configuration retains its unpaired nature, resembling the ground state, but the two electrons now occupy distinct antibonding orbitals. Conversely, in the triplet excited state, the energy level surpasses that of the excited singlet state, and the electrons reside in separate antibonding orbitals with paired spins.

The generation of singlet oxygen typically occurs through energy transfer to molecular oxygen in its triplet ground state, $^3O_2$. This process is facilitated by photosensitizers that absorb light at specific wavelengths, transferring energy from their excited state to $^3O_2$ and activating the formation of $^1O_2$.

Singlet oxygen is notable for its extended lifespan in the air, which lasts approximately 2.80 s at 23 °C under 1 atm. During this time, it is capable of diffusing about 0.992 cm through the air, although its diffusion length shrinks to 200 nm when submerged in water.

Within the field of carbon-based nanomaterials, the well-documented phenomenon of $^1O_2$ generation through photostimulation has been extensively explored. It is particularly pronounced in various nanostructures, including fullerenes [115, 116], graphene [117-119], and carbon nanotubes [120], where these materials function as sensitizers, producing singlet oxygen.

Polythiophene-derived GQDs [121] possess the capability to operate as photosensitizers. This characteristic stems from their adeptness in propelling ground-state electrons into an excited singlet state. The ensuing trajectory encompasses intersystem crossing (ISC), directing these electrons toward a more stable excited triplet state through an energy transfer process involving oxygen molecules. This unique mechanism culminates in the generation of $^1O_2$, distinguished by its heightened reactivity attributable to the unique spin pairing of the two electrons within the π^* antibonding orbitals.

In these systems, the singlet oxygen quantum yield (QY,) a metric quantifying the ratio of produced $^1O_2$ per individual incident photon, consistently maintains a level below 1.

Diverging from conventional sensitizers such as porphyrins and phthalocyanines, which rely on energy transfer from their excited triplet state to $^3O_2$ for $^1O_2$ generation, GQDs prepared from polythiophene show a distinctive multistate photosensitization mechanism. The singlet oxygen QY surpassing 1 in these GQDs indicates a novel excitation mechanism. This elevated QY is elucidated through a multistep process wherein energy transfer to $^3O_2$ transpires through two distinct decay pathways, ultimately amplifying the QY of $^1O_2$.

GQDs derived from phthalocyanines [122] exhibit the generation of singlet oxygen upon visible light excitation. These GQDs absorb light in the 400–700 nm range, emitting light peaking at 680 nm in the deep red spectrum. Similarly, CDs prepared via solvothermal reaction [123] can initiate $^1O_2$ generation upon exposure to visible light, presenting practical applications in antibacterial photodynamic inactivation.

The capacity of CDs to induce ROS hinges on distinct photoreaction pathways, where efficient energy transfer to $^3O_2$ does not necessarily correlate with electron transfer capability. The adoption of nitrogen doping emerges as a widely applicable strategy for modifying CD properties.

The introduction of nitrogen often accompanies the emergence of oxygen functional groups, leading to significant alterations in material properties. Nitrogen doping within GQDs results in diverse chemical bonding configurations within the graphene layers, including graphitic-N, pyridinic-N, pyrrolic-N, as well as edge and surface amines.

Typically, higher nitrogen contents induce a redshift in both absorption and emission spectra, coupled with changes in electronic properties compared to undoped carbon dots.

Utilizing computational modeling, it has come to light that graphitic-N sites contribute to a redshift by effectively narrowing the HOMO-LUMO gap. This redshift phenomenon stems from the filling of unoccupied π * orbitals within a conjugated system, utilizing excess electrons for this purpose. In contrast, pyrrolic and pyridinic-N sites induce a blueshift, presenting an opposite trend. The distinctive impact of these nitrogen sites underscores the critical importance of the positioning of nitrogen atoms within the graphenic structure. Wu et al.[110] have undertaken a comprehensive exploration, systematically investigating the diverse effects of various N-sites within GQDs on the generation of ROS[81, 124]. They observe that those radicals generated from GQDs synthesized via a hydrothermal route using citric acid and ethylenediamine were intricately linked to the number of nitrogen sites, displaying a distinctive pattern. Specimens crafted with escalating amounts of ethylenediamine, the nitrogen source, showed an elevated fluorescence QY and extended decay time, corresponding to the increasing N content.

However, the photosensitization effect does not follow a linear progression, revealing a peak at a specific composition (citric acid: ethylenediamine = 1:1, in molar ratio). The presence of N-pyridinic species escalates with the rising concentration of ethylenediamine, while N-pyrrolic and N-graphitic species witness a reduction. The maximal production of ROS aligns with the highest content of pyrrolic-N and graphitic-N sites, registering a minimum in pyridinic-N sites. These fluctuations in N-site composition precisely reflect the GQDs' efficacy in ROS production, particularly $^1O_2$ and $O_2^{\cdot-}$, without any production of hydroxyl radicals.

The oxygen adsorption energy on various nitrogen-doped structures exhibits a distinct order: pyrrolic N demonstrates the highest adsorption energy, followed by pyridinic N and graphitic N.

Moreover, pyrrolic and graphitic nitrogen sites act as electron donors. These sites facilitate electron transfer to the adsorbed O_2, resulting in the generation of superoxide anions ($O_2^{\cdot-}$). This mechanism not only yields singlet oxygen but also prompts the formation of superoxide anions. The presence of pyrrolic-N sites is indicative of a preference for oxygen adsorption, thereby facilitating subsequent electron transfer.

Functional oxygen groups situated on the surface of GQDs play a pivotal role in diverse catalytic functions. In a comprehensive study by Qu et al. [125, 126], three distinctive functional groups were identified: ketonic carbonyls (-C=O), hydroxyl (-C-OH), and carboxylic groups (O=C-O-). Specifically, the -C=O group acts as an active site for H_2O_2 decomposition, -C-OH facilitates substrate binding, and O=C-O- acts as an inhibitory site for the reaction [81, 127]. The selective removal of these groups has allowed for the discernment of the primary contributor to the generation of ROS, with the ketonic group emerging as the predominant factor [81, 126].

The intricate process of ROS formation by GQDs involves a multifaceted interplay of factors. While the lifetime of the triplet excited state has an impact on energy transfer to $^3O_2$, empirical data suggest that other parameters exert a more substantial influence on ROS generation. The efficient absorption of oxygen by GQDs is indispensable for the necessary energy and electron transfer. The presence of diverse oxygen-functional groups on the surface, especially the ketonic carbonyl groups, significantly shapes ROS generation by favoring the formation of hydroxyl radicals.

Furthermore, the intentional introduction of heteroatoms, such as chlorine [128], through the process of doping CDs, positively influences energy transfer to oxygen, thus making an additional substantial contribution to the overall generation of ROS.

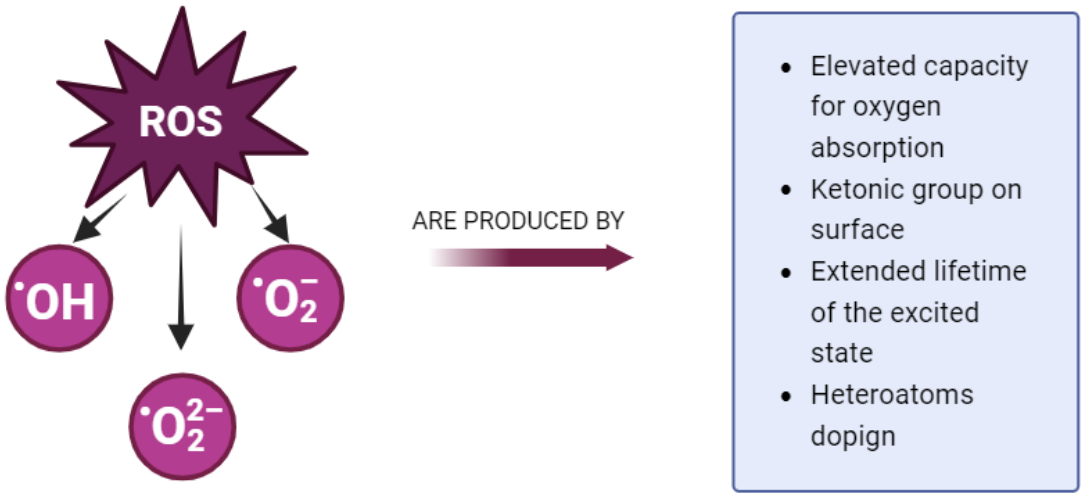

Figure 10: Mechanisms of ROS generation in GQDs.

CDs, in addition to acting as oxidizing agents, exhibit antioxidant properties by donating a hydrogen atom or through electron transfer.

Antioxidants fall into two main categories [129]: enzymatic, such as superoxide dismutase [130], catalase [130, 131], peroxidase [132], and ascorbate peroxidase [133]; and nonenzymatic, including polyphenols [134], phenolic acids [135], flavonoids [136], and ascorbic acid [137, 138]. CDs belong to the nonenzymatic group of radical scavengers [139].

The radical scavenging efficacy of CDs exhibits substantial variability based on their composition and structural nuances. Their performance intricately depends on the specific types of radicals involved.

1.4.3 RNS scavenging mechanisms

CDs have radical-scavenging properties against ROS and nitrogen-reactive species (RNS) [140, 141]. including NO· and NO_2·, which could potentially interfere with cellular processes. The assessment of scavenging activity involves the application of 1,1-Diphenyl-2-picrylhydrazyl radical (DPPH•), a stable nitrogen-centered free radical [142]. DPPH•, owing to its electronic configuration, readily accepts an H• radical, resulting in the formation of the stable diamagnetic DPPH-H complex. Scavenging efficacy is obtained by measuring the attenuation in the ESR signal generated by a free radical in the presence of CDs.

S and N-doped CDs, synthesized hydrothermally at 200 °C using garlic as a natural precursor, exhibit scavenging activity towards RNS [143]. While the study reports the scavenging effectiveness, it lacks specifics regarding garlic composition and origin, raising questions about process reproducibility. The suggested mechanism involves hydrogen transfer from CDs surface groups to DPPH•, facilitated by carboxyls (-COOH), hydroxyls (-OH), and amino (-NH_2, -NH) groups. The unpaired electrons on the CDs surface contribute to scavenging through resonance within aromatic domains or chemical bond rearrangement. Additionally, electron transfer mechanisms involving nitroxide radicals quench the blue fluorescence of CDs.

GQDs have also been explored as potential scavengers of RNS [81, 144]. The presence of sp^2 bonds and unpaired electrons suggests favorable radical scavenging activity, as tested by ESR. Variability in RNS scavenging performance within this class of CDs is influenced by the synthesis method. Improved scavenging activity is observed in CDs doped with non-metallic heteroatoms such as Mn and P [81, 145]. The effect of doping on RNS scavenging has been further investigated by comparing GQDs, N-doped GQDs, and GQDs doped with dual heteroatoms, S and N [81, 146]. However, only the N-doped sample demonstrates detectable RNS activity, but lower than that of Vitamin C. Interestingly, dual doping with N and S atoms diminishes RNS scavenging activity. Multiple doping with N, S, and P atoms does not enhance RNS scavenging either [81, 147].

Exploring the antioxidant properties of graphene reveals structure-dependent radical scavenging activities. Graphene oxide (GO), reduced graphene oxide (rGO), and few-layer graphene (FLG) exhibit varying radical scavenging activities against RNS [81, 148].

In GO, the presence of a low number of phenolic OH groups is notable. Many antioxidants are phenolic compounds, and their radicals benefit from stabilization through resonance structures. In this configuration, unpaired electrons can reside on the oxygen atom or on ortho or para carbons on the adjacent aromatic ring. In GO, most hydroxyls are expected to be located out-of-plane concerning the basal sites. The oxidation of the C=C double bond results in the formation of sp^3 sites lacking the

adjacent conjugated structure that stabilizes the radical resonant electron. Phenolic OH groups in GO are anticipated to be primarily found at the structure edges, not in the basal plan, thus diminishing the proton donor capability of the graphene oxide structure.

A direct demonstration of the role played by phenolic groups as active sites for proton transfer was achieved by reducing a CQD initially rich in oxygen functional groups (OFGs) (C=O, C-OH, and COOH). The reduction using $NaBH_4$ converts C=O to C-OH, creating phenol-like groups in the dot [81, 135]. Although carboxyl groups and total oxygen remain unaffected by the reduction, approximately 75% of OFGs change to C-OH during the process. Unlike GQDs that still contain carboxylic species, the DPPH• test revealed that substantial amounts of phenol-like groups enhance radical scavenging action. Theoretical calculations underscore the importance of adjacent oxygenated groups in modulating the OH bond dissociation energy of phenol-like groups. Moreover, the presence of close carbonyl groups can reduce the proton donor activity of phenol-like species. Thus, effective antioxidant CQDs should ideally be rich in phenolic groups while avoiding or limiting the presence of carbonyl groups.

Ruiz et al. [149], undertook a comparative assessment of GQDs derived through diverse methodologies, each meticulously characterized . Three GQD variants were synthesized: one through the oxidative exfoliation of carbon black nanoparticles (GQDv), another employing hydrothermal treatment (HT) of glucose in ammonia (GQDg), and a third via HT treatment of pyrene (GQDp). These GQDs showed distinct sp^2 carbon contents, notably with GQDp featuring a significantly higher content. The varied compositions resulted in differing performances in radical scavenging. GQDp exhibited notably superior capabilities in scavenging nitrogen reactive species compared to hydroxyl radicals. All systems fell short as scavengers of RNS in comparison to the standard antioxidant, ascorbic acid (AA), while excelling in the case of ·OH. The heightened scavenging properties of GQDp against nitrogen-reactive species were ascribed to the presence of functional groups at the edge sites (-OH and $-NHNH_2$) in conjunction with an extended network of sp^2 carbon atoms. These functional groups served as hydrogen donors, while the graphenic structure played a pivotal role in stabilizing and dispersing the free electrons, a critical characteristic elucidated through comparative analyses with GQDv and GQDg.

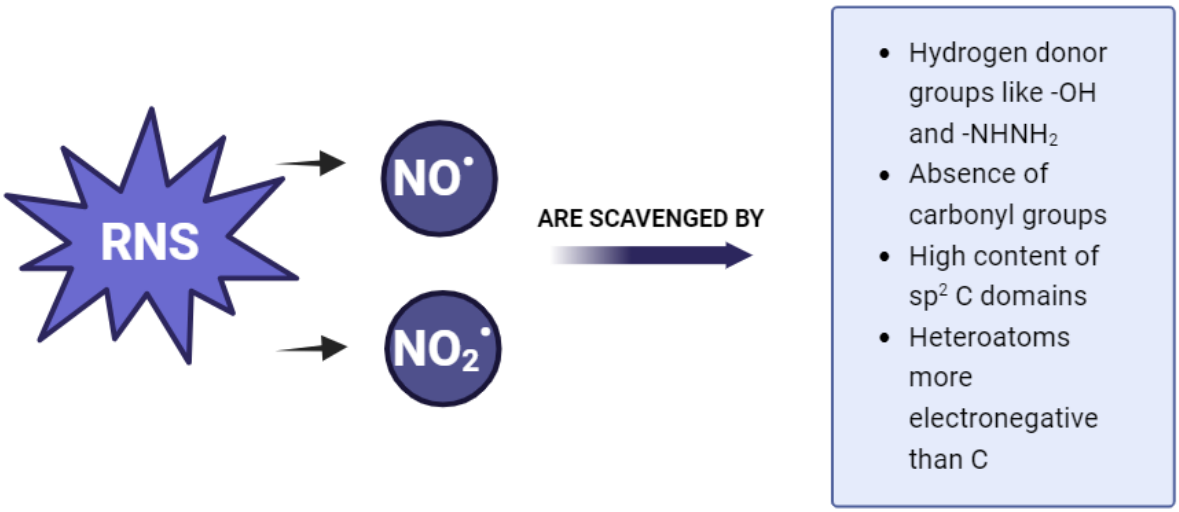

Figure 11: RNS scavenging mechanisms of CNDs and GQDs.

1.4.4 ROS scavenging mechanisms

The scavenging mechanism of OH in GQDP is attributed to the presence of larger C sp^2 domains. Some studies have demonstrated OH scavenging activity even in GQDg with smaller C sp^2 domains, achieved through nitrogen doping. This occurs because nitrogen enables the formation of radical adducts and electron transfer. Highly oxidized GQDv nearly lose their scavenging capacity. The coexistence of a graphene-rich structure with sp^2 domains and surface groups acting as proton donors promotes radical scavenging action [149].

The presence of heteroatoms increases sp^3 sites, and the unbalanced distribution of electron charges in carbon hexagonal rings facilitate interactions between nanoparticles and radicals. Various methods are employed to test antioxidant action, with the most common involving the generation of hydroxyl radicals through the Fenton reaction, based on the oxidation of iron (II) by hydrogen peroxide. Alternatively, TiO_2 is dispersed in a solution and irradiated with UV light [144]. The use of 5,5-Dimethyl-1-pyrroline N-oxide (DMPO) forms the spin adduct DMPO/OH to trap hydroxyl radicals, and electron spin resonance (ESR) spectra are utilized to quantify radical scavenging activity.

Numerous experiments have been conducted, both in vitro [150, 151]and in vivo [152, 153], to assess the efficacy of selenium atoms in reducing free radicals in CDs. CQDs are synthesized with a chemical structure that blends amorphous and crystalline features, akin to the spacing between different layers in bulk graphene.

In the work of Chen et al. [151], two computational models were employed, consisting of structures composed of four and six carbon rings, each containing selenium atoms. The carbon regions exhibit a balanced distribution of both sp^2 and sp^3 hybridized carbons. Selenium-doped sites act as electron donors, transferring electrons to radicals, while the "holes" generated by these transfers actively participate in the transformation of radical adducts.

Among GO, rGO, and FLG, FLG exhibits the highest radical scavenging activity, followed by rGO. The one with the least antioxidant power is GO, as it has less extensive sp^2 domains. Indeed, sp^2 sites are considered the primary scavenging sites, functioning through electron transfer or adduct formation [148].

CDs have been investigated as scavengers of $O_2^{\cdot-}$, which form through the one-electron reduction of O_2. An excess of $O_2^{\cdot-}$ can accelerate aging processes and the proliferation of cancer cells through lipid peroxidation. In biological systems, $O_2^{\cdot-}$ is typically scavenged by antioxidant enzymes through disproportionation to H_2O_2 and O_2. Reports on the radical antioxidant activity of CDs against $O_2^{\cdot-}$ are generally lower compared to RNS and hydroxyl radicals. In general, CDs do not perform well in reducing $O_2^{\cdot-}$, with a few exceptions. Similarly, graphene materials, such as GO, have demonstrated only modest scavenging activity against superoxide, especially when compared to ascorbic acid. In this context, the system's capability to adsorb oxygen molecules is crucial, emphasizing the importance of a well-designed system.

An instance of antioxidant-prooxidant CD systems involves laser ablation of graphite, surface-passivated with poly(propionyl ethyleneimine-co-ethyleneimine) or PEG 1500 [154]. When exposed to blue lamp illumination (390–470 nm), these dots produce ROS, including $^1O_2$. Conversely, when not directly exposed to visible light, the CDs primarily function as scavengers of $^1O_2$. GQDs obtained through oxidation and cutting exhibit a broader oxidative-antioxidative (Ox-AntiOx) activity. They act as free radical scavengers against $\cdot OH$, $O_2^{\cdot-}$, and RNS. Illumination with a Xenon lamp (450 nm) induces the generation of $\cdot OH$, $O_2^{\cdot-}$, and $^1O_2$. A similar oxidant activity is observed in chlorine-doped GQDs prepared via an electrochemical method [128]. These GQDs scavenge $\cdot OH$ and RNS, while generating $O_2^{\cdot-}$ upon Xenon lamp illumination. However, the formation of other ROS, such as $\cdot OH$ and $O_2^{\cdot-}$, has not been observed.

These observations highlight the nuanced interplay of electronic configurations and energy dynamics within molecular oxygen, providing valuable insights into its behavior under severalconditions.

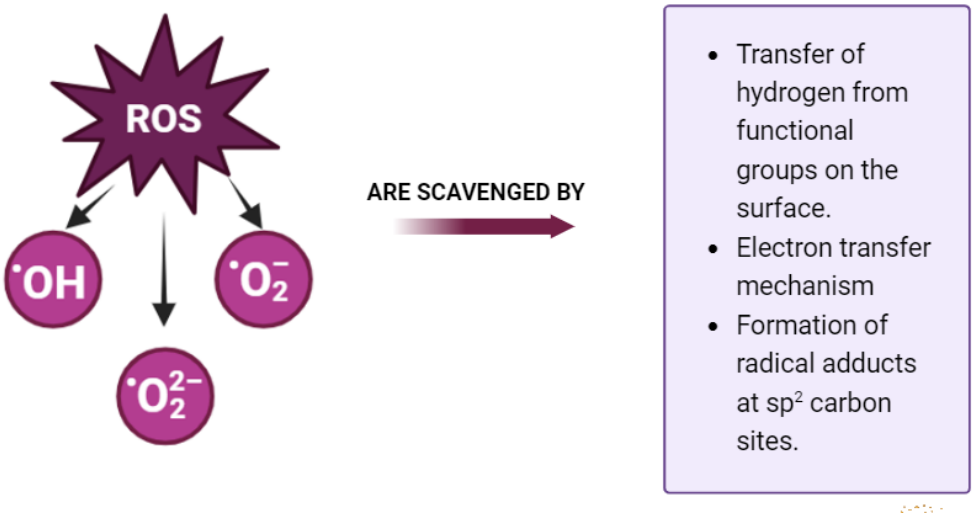

Figure 12: ROS scavenging mechanisms.

The study of Gao et al. [132] elucidates the interplay of functional characteristics and the synthesis process employed for CDs with inherent superoxide dismutase (SOD) nanozyme properties. Hydroxyl, and carboxyl groups within CDs form bonds with superoxide anions. The oxidation of the carbonyl groups causes the release of oxygen with the reduction of CDs. This reduced state is seamlessly engaged in a redox cycle, by another superoxide anion, which produces hydrogen peroxide (H_2O_2). These nanoenzymes have a higher affinity for cells and mitochondria that are subject to oxidative stress. This underscores the efficacy of SOD nanoenzymes in mitigating intracellular ROS levels. In vivo application results in an antioxidant action for neurons subject to oxidative stress induced by cerebral ischemia.

CDs synthesis occurs when larger carbon structures, including graphite powder [155], carbon black [156], and activated charcoal [157], undergo oxidative modification through a mixture of nitric acid and sulfuric acid at a ratio of 1:1. Fundamental to their catalytic ability is the preservation of a substantial content of C=C bonds, that indicates a system of π electrons. This not only facilitates electron transfer but also stabilizes intermediates harboring unpaired electrons, thereby ensuring the heightened SOD enzymatic activity intrinsic to C-dots.

The synthesis introduces an essential perturbation – oxidative etching – that fragments the relatively complete π electron system of the original carbon materials. Oxygen-containing functional groups (carboxylic, hydroxyl, and carbonyl) are obtained on the surface of CDs. At the same time, the initially ordered sp^2 network structure transforms into a sp^2-sp^3 dynamic hybrid nanostructure.

Weak interactions, including static electricity, hydrogen bonds, and van der Waals forces, are formed between the oxygen-containing surface groups on the CDs, which catalyze redox reactions with superoxide anions.

By selectively deactivating carboxylic, hydroxyl, and carbonyl groups, it has been observed that hydroxyl and carboxyl groups constitute essential components of the active sites in nanoenzyme

structures. The π-electron system of CDs also proves to be crucial. Although multiple factors influence the SOD-like activity of CDs nanozymes, the catalytic site is identified as the carbonyl groups, with hydroxyl groups playing an essential role in reactant binding.

The entire SOD-like catalytic cycle, as represented by Equations (2), involves two elementary reactions: an oxidation reaction (Equation (3)) and a reduction reaction (Equation (4)). The conversion of a CDs carbonyl group (denoted as π-C = O) to a hydroxyl group (denoted as π-OH) occurs through the oxidation of an $HO_2^{\bullet}$ free radical, resulting in the production of an O_2 molecule. Conversely, the reduction of an $HO_2^{\bullet}$ free radical transforms a hydroxyl group into a carbonyl group, producing an H_2O_2 molecule.

$$O_2^{\cdot-} + H_2O \rightarrow HO_2^{\cdot} + OH^- \quad \textbf{(1)}$$

$$2HO_2^{\cdot} \rightarrow O_2 + H_2O_2 \quad \textbf{(2)}$$

$$HO_2^{\cdot} + O = (C - dot) = O \rightarrow O_2 + HO - (C - dot) - O^{\cdot} \quad (3)$$

$$HO_2^{\cdot} + HO - (C - dot) - O^{\cdot} \rightarrow H_2O_2 + O = (C - dot) = O \quad (4)$$

Calculations demonstrate that, in comparison to CDs nanozymes lacking hydroxyl groups, the binding energy between $HO_2^{\bullet}$ and CDs nanozymes with hydroxyl groups is significantly lower (−0.65 eV vs. −0.54 eV, as depicted in Fig. 4c and d). This indicates that hydroxyl CDs exhibit a stronger ability to capture $HO_2^{\bullet}$ free radicals. Consequently, these findings highlight the role of hydroxyl groups as the key structural element in the SOD-like catalytic activity site of CDs nanozymes [158].

CDs exhibit a dual functional nature, demonstrating both oxidative and antioxidative actions, a duality intricately linked to the modulation of their chemical structure. The interplay between surface functional groups and the molecular configuration of CDs allows them to act as catalysts in oxidative reactions while concurrently playing a protective role through antioxidative capabilities. This multifaceted behavior is precisely tailored by the chemical composition and molecular interactions present on their surface.

2 Aim of the work

The aim of this thesis work is the synthesis of carbon dots with scavenging capabilities. A sustainable source, specifically garlic biomass, was employed for this purpose. The objective is to combine the antioxidant and anti-inflammatory properties of garlic with the optical characteristics of carbon dots. This synergy is intended to produce an innovative material that fully exploits the beneficial qualities of garlic, in conjunction with the distinctive features of carbon dots, to effectively address oxidative stress.

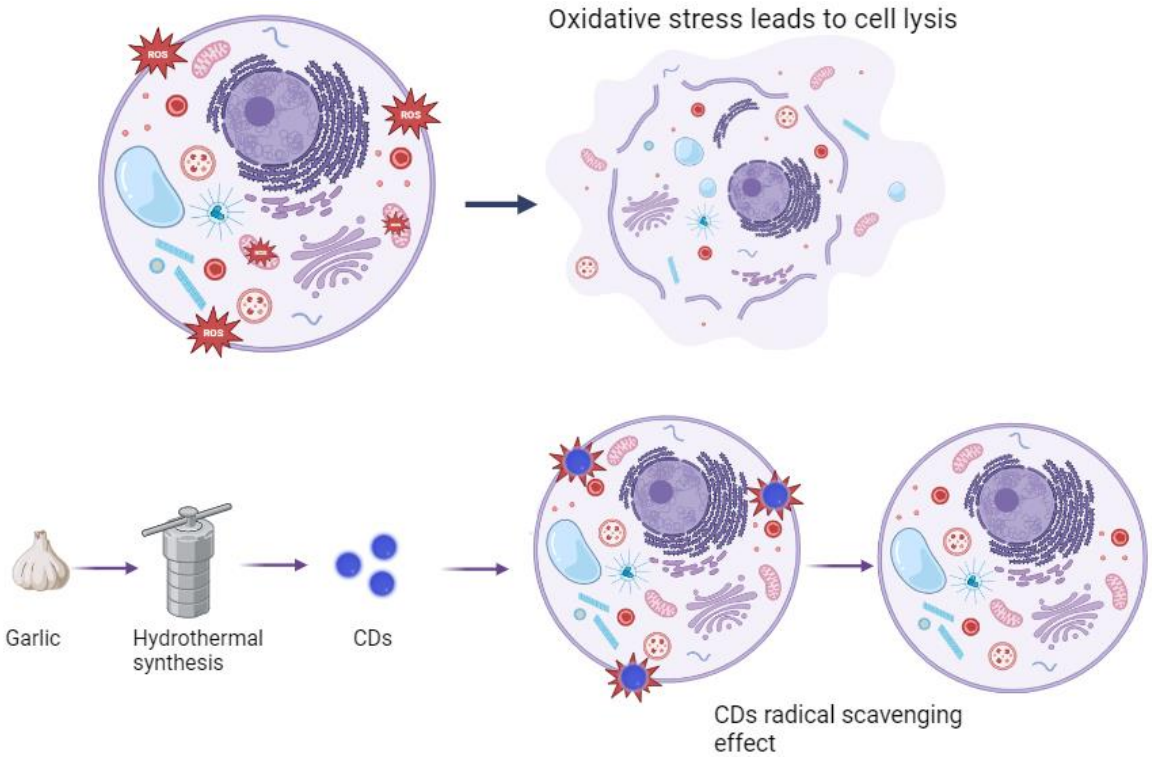

Graphical abstract: Oxidative stress can lead to cell death. CDs are produced with a hydrothermal synthesis from garlic. They act as radical scavengers, allowing cell recovery.

3 Materials and methods

3.1 Materials

In this thesis work, CDs were synthesized using lyophilized garlic as the starting material. A Carrefour branded lyophilized garlic in granular form was procured (30/09/25 L01256Z). The synthesis process involved the utilization of sulfuric acid (H_2SO_4) purchased from Sigma Aldrich and caustic soda (NaOH) from Texas.

Trypsin – EDTA Solution 10x was purchased from Sigma-Aldrich(T4174-100mL). It was diluted to 1x in Dulbecco Phosphate-Buffered Saline (DPBS) obtained from 10x concentrated DPBS also purchased from Sigma-Aldrich (P5493-1L) diluted in sterile deionized water (ddH_2O).

Gibco RPMI 1640 Medium [Thermo-Fisher, A4192301], was supplemented with:

- 10% Fetal Bovine Serum (FBS) [Sigma-Aldrich, F9665]
- 1% Penicillin/Streptomycin [Sigma-Aldrich, P4333-100mL]

3-(4,5-dimethylthiazol-2-yl)-2,5-diphenyltetrazolium bromide (MTT) [Sigma-Aldrich, M2128], was suspended at the concentration of 5 mg/mL in DPBS , and diluted to 0.5 mg/mL with RPMI before use.

For cytocompatibility assay, adenocarcinoma cell lines, A549, constitutively expressing green fluorescent protein (GFP) were kindly provided by Valentina Monica, Department of oncology, University of Turin.

All materials were used without any further purification.

3.2 Methods

3.2.1 Synthesis of CDs

The synthesis of CDs involved a hydrothermal process conducted in an autoclave, utilizing garlic as the primary biomass. To optimize the reaction and attain an equilibrium between yield, fluorescence emission, and carbonization degree, a series of five syntheses were systematically performed. Variations in process conditions, which are time and temperature, were implemented, comprising syntheses at 180°C for 3 hours, 180°C for 6 hours, 200°C for 3 hours, 200°C for 6 hours, and 220°C for 3 hours.

For each specified reaction condition, 2.00 g of lyophilized garlic were weighed using a Radwig balance and introduced into a Teflon reaction chamber, along with 10 ml of deionized water. The Teflon chamber was subsequently placed within a metal autoclave, sealed, and enveloped with aluminum foil to ensure uniform temperature distribution. Then it was positioned atop the REC Digital Heating Ceramic Plate by VELP Scientifica, situated under a fume hood, setting the reaction temperature for the reaction time.

Upon determining the optimal reaction conditions, 1 mL of H_2SO_4 was introduced into the autoclave with garlic and water to augment reaction yield for scalability. After the established reaction period, the

heating plate was deactivated, and the autoclave was allowed to cool in a water bath. After the cooling phase, the autoclave was opened within the fume hood, and NaOH was added to neutralize the acidic nature of the sulfuric acid, thereby facilitating subsequent filtration.

3.2.2 Purification of CDs

CDs were obtained through a filtration process followed by dialysis. A 90 mm diameter Whatman filter was employed, placed inside a Büchner funnel mounted on a tail flask connected to a vacuum pump. Upon establishing a vacuum, the autoclave contents, combined with 5 mL of deionized water, were carefully introduced into the Büchner funnel, resulting in the collection of a 50 mL solution containing the CDs.

An 8 cm segment of an 8000 Da molecular weight cut-off dialysis membrane was sectioned. One end was securely sealed using a plastic clamp, and the membrane was immersed in a 250 mL beaker containing deionized water. After a 5–10-minute waiting period, the sealed end was opened, allowing the 50 mL solution to be poured. Subsequently, the other end of the membrane was sealed, and a small magnet was introduced into the water. The beaker was then placed on the VELP Scientific magnetic stirrer at a moderate speed to prevent vortex formation. The dialysis process was carried out for 3 days, with regular water changes every 24 hours.

The contents of the dialysis bag were then carefully transferred to a 100 mL glass beaker and desiccated in a Kenosistec oven at 80 °C for 24 hours. After drying, carbon dots were scraped from the bottom and walls of the beaker.

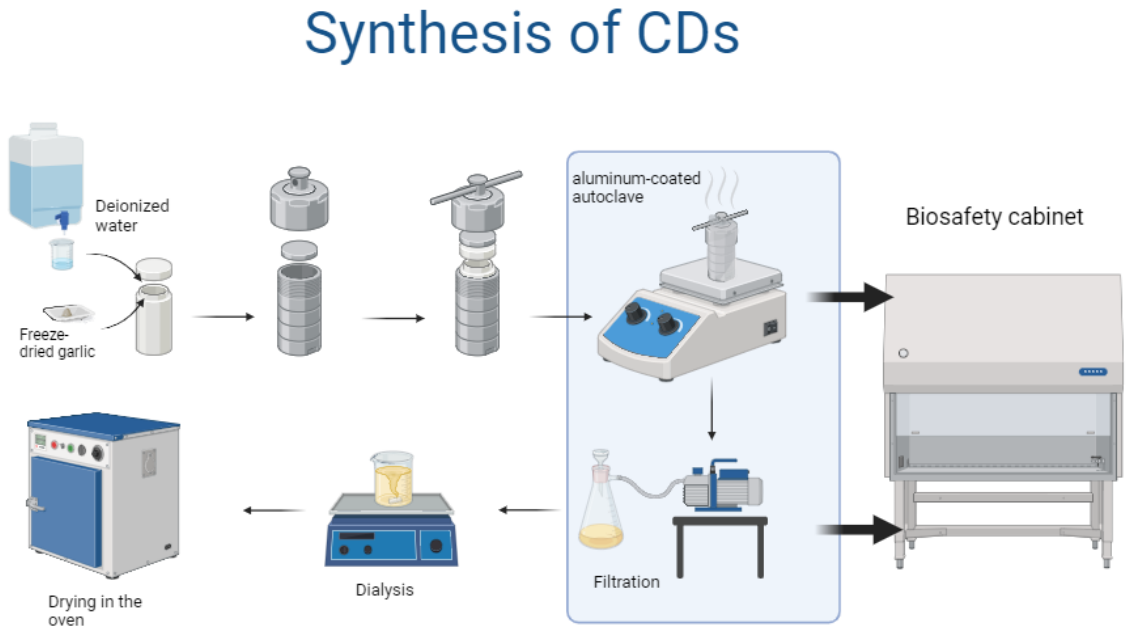

Figure 13: Synthesis steps to produce garlic-derived CDs.

3.2.3 Characterization of CDs

Fluorescence emission analysis was conducted using the Perkin Elmer LS 55 fluorescence spectrometer. Five solutions of deionized water and CDs at a concentration of 0.2 mg/mL were prepared and transferred into quartz cuvettes. After activating the computer, parameters were configured, and the excitation wavelength was varied from 260 to 340 nm with 10 nm increments between measurements. The scanning speed was set at 50 nm/min.

For the chemical composition studies of CDs synthesized, a Nicolet 5700 FT-IR spectrometer by ThermoFisher Scientific was employed.

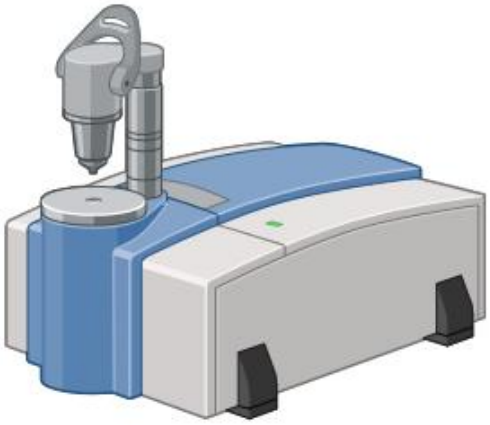

Figure 14: FT-IR spectrometer.

Initializing the computer, an initial acquisition was performed with direct deposition of the sample onto a diamond mirror without the use of solutions or salt pellets. Preliminary signal acquisition was performed before sample deposition to allow subtraction of the background signal from that of the sample. This initial acquisition captured the signal arising from stretching vibrations along the bonding axis of water and carbon dioxide molecules, typically present in the instrument's environment.

Morphological analyses were carried out employing AFM and TEM. UV-Vis spectroscopic analysis was conducted, and a comprehensive characterization of the chemical structure of the CDs was achieved through thermogravimetric analysis (TGA).

TGA analyses were performed using a Netzsch TG 209 F3 Tarsus thermo-microbalance while heating under a nitrogen flow of 40 ml/min from 40 to 800 °C at a rate of 20 °C/min.

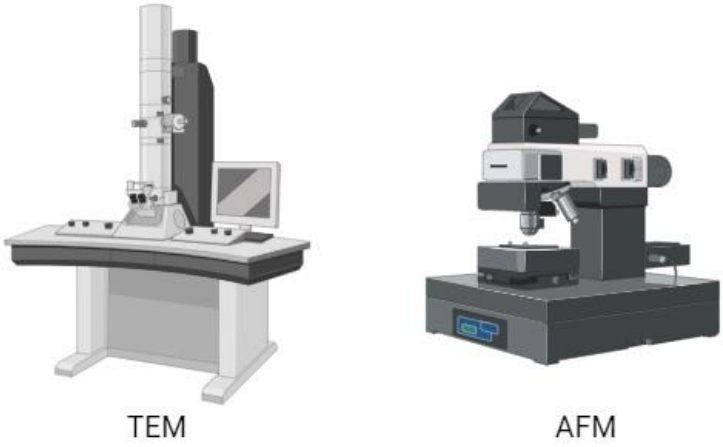

Figure 15: Transmission Electron Microscope and Atomic Force Microscopy.

For the AFM analysis, a silicon wafer was cleansed with acetone to form a superficial oxide layer and left to dry at room temperature for 3 days. Subsequently, a solution of CDs at 0.2 mg/mL was prepared. The silicon wafer was then sectioned into small pieces, and drops of the solution were deposited. After the drops dried, microscopic analysis was performed. The images were acquired using the Brocher Innova AFM in tapping mode. The probe used was the TAP 300 Al-G from Budget Sensors, operating at a resonance frequency of 300 kHz with an apex diameter of less than 10 nm. A 30 nm thick aluminum reflective coating is present on the detector side of the cantilever. The scan rate was set at 0.5 Hz. The acquisitions were conducted under ambient conditions. Images were processed with Gwyddion software.

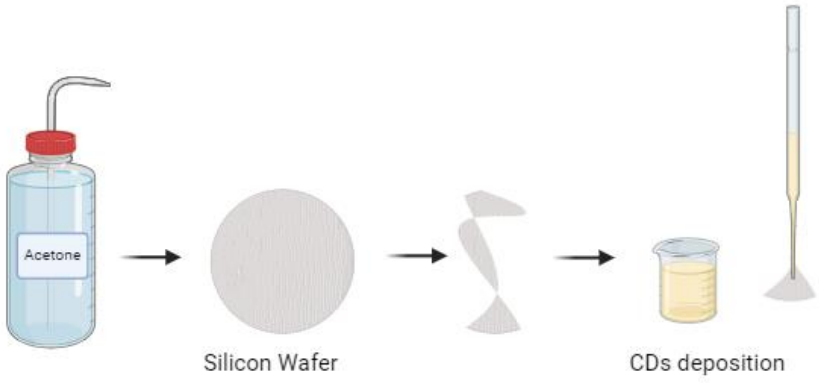

Figure 16: Steps for Sample Preparation for AFM.

3.2.4 UV-Vis Spectroscopy

To perform UV-Vis spectroscopy analysis and assess the antioxidant capacity of CD nanoparticles, the procedure begins with the preparation of sample solutions. 3 mg of CDs are accurately weighed using the Iteco Engineering balance and added to 20 mL of deionized water.

Subsequently, solutions of red dye, extracted from natural cochineal are prepared to obtain three progressive solutions (SOL1, SOL2, SOL3) through dilutions. SOL1 consists of 10 mg of dye in 10 mL of water, SOL2 is obtained by withdrawing 3 mL from SOL1 and adding 27 mL of water, while SOL3 is derived from SOL2 by withdrawing 2 mL and adding 18 mL of water. Dilutions continue until a dye concentration of 10 mg/L in 20 mL is achieved.

The use of a graduated pipette with a three-valve rubber bulb facilitates each withdrawal.

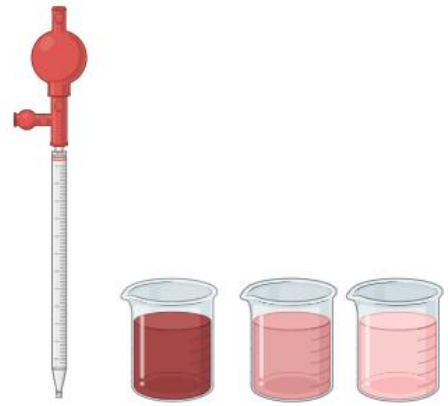

Figure 17: 10 mL graduated pipette with three-valve rubber pump; Different concentrations of the solution of red dye, cochineal extract, and distilled water.

To subject the samples to UV irradiation, a rudimentary chamber lined with aluminum foil was created, positioning the VIQUA S463RL Lamp through lateral openings on a cardboard box. During irradiation, this box is placed over the samples on a magnetic stirrer.

Figure 18: Experimental set-up with VIQUA S463RL lamp.

To assess the dye preservation capability in the presence of CDs, it is necessary to determine the irradiation time causing maximum degradation. The calibration curve of the non-irradiated dye with three solutions irradiated for different durations was compared. The calibration curve is constructed

using four solutions of water and dye with diluted concentrations (0.01 mg/mL) through 1:2, 1:4, and 1:8 dilutions.

Solution	Dilution	Concentration (mg/mL)
C1	Start	0.01000
C2	1:2	0.00500
C3	1:4	0.00250
C4	1:8	0.00125

Table 1: successive dilutions of the solution of water and dye to build the line calibration of the dye not irradiated by the UV lamp.

Subsequently, the three previously obtained solutions were subjected to increasing UV irradiation periods: 10 minutes (S1), 20 minutes (S2), and 30 minutes (S3), as depicted in Table 2.

Solution	Concentration (mg/mL)	Irradiation time (min)
S1	0.01	10
S2	0.01	20
S3	0.01	30

Table 2: Irradiation of the dye solution with a concentration of 0.01 mg/mL at different times

Then, seven samples of CDs in dye solution and distilled water at a concentration of 10 mg/L were composed. Each sample contained 3 mg of CDs in 20 mL of solution and is left on the stirrer at low speed for 24 hours before proceeding with UV-Vis spectroscopy analysis, both pre-and post-irradiation.

During UV-Vis analysis, each sample is placed in a 1 cm quartz cuvette. This detailed approach allows for the evaluation of the dye's preservation capacity in the presence of CDs, with the irradiation time considered a critical variable for dye degradation.

Figure 19: Quartz cuvette.

3.2.5 CDs preparation for *in vitro* analysis

The preparation of the test solution involved weighing 20 mg of CDs and suspending them in 1 mL of RPMI in a vial, obtaining a concentration of 20 mg/mL.

1 mL was aliquoted into an aluminum foil-covered Falcon tube, to which 9 mL of culture medium were added, achieving a concentration of 2 mg/mL. To homogenize the solution with 2 mg/mL CDs, sonication for 10 min was performed.

Dilutions were made to reach concentrations of 1 mg/mL and 0.5 mg/mL for 6 or 3 wells, depending on the fixation of 1 or 2 time points.

3.2.6 MTT assay

To assess the cytotoxicity of CDs, MTT analysis is performed. Cells are cultured on 10 cm Petri dishes in supplemented RPMI until they reach a confluence of 70-80%, then they are detached with 1x Trypsin-EDTA and count by Burker chamber after staining with erythrosine to mark dead cells.

For the experiment, $4x10^5$ cells are seeded in each well of a 48-multiwell plate and grown overnight. Then, three culture conditions are determined according to CDs concentration, i.e. 1 mg/ml or 0.5 mg/ml. Cells culture with supplemented RPMI are used as positive control.

Using a ZOE Fluorescent Cell Imager system, photos are taken before adding the CDs.

For the assay, DPBS is used to rinse the wells with CDs, and 700 µL of 0.5 mg/mL MTT is added. After 2 hours on incubation, MTT solution is aspirated, and 700 µL of DMSO is added. The formed salts are mechanically dissolved, and absorbance is read at 570 nm (reference wavelength650 nm).

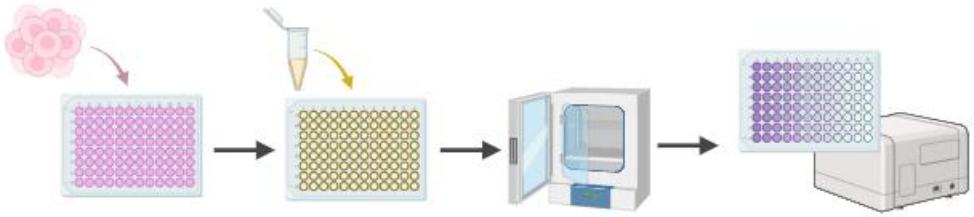

Figure 20: MTT assay steps.

4 Results and discussion

4.1 Characterization of CDs

4.1.1 Fluorescence Spectroscopy

To evaluate the optimal reaction conditions, fluorescence analysis was conducted for each synthesis at temperatures ranging from 180 °C to 220 °C, with durations of 3 or 6 hours. In Figure 21, fluorescence intensity is plotted against wavelength. The legend indicates the excitation wavelengths.

In Figure 22, emission energy is presented relative to excitation energy. The legend reports the emission peaks.

In all the samples it is observed a blue fluorescence emission with an excitation-independent mechanism.

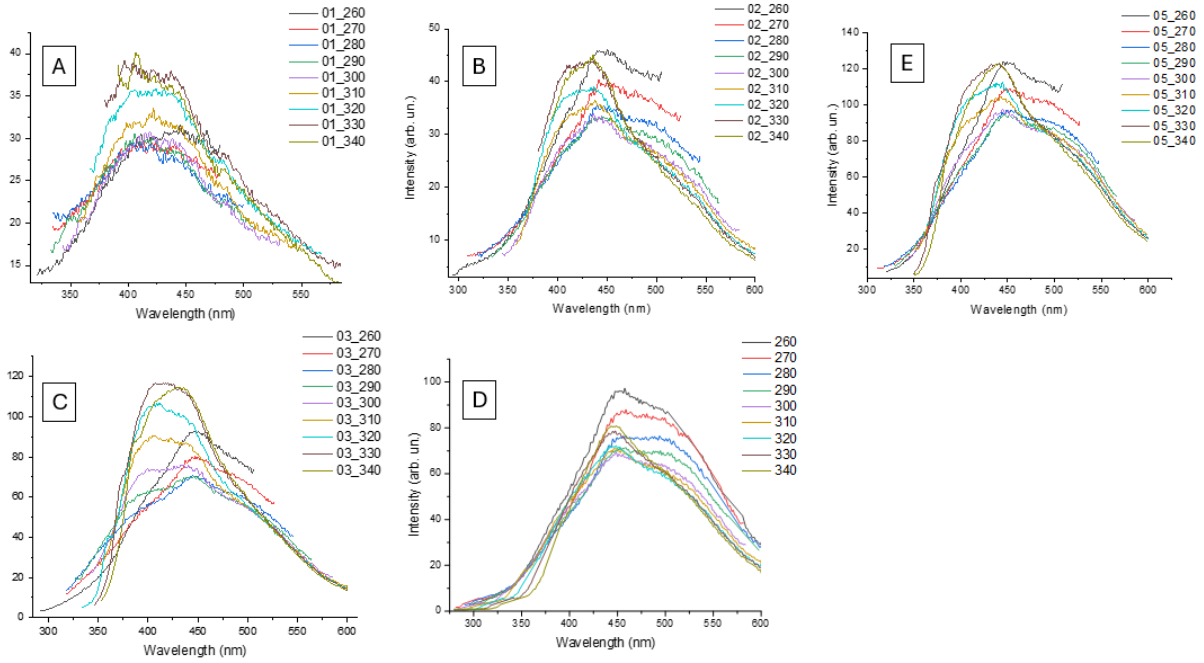

Figure 21:Fluorescence intensity of CDs synthesized at various time and temperature conditions: A)180 °C for hours; B) 180 °C for 6 hours; C) 200 °C for 3 hours; D) 200 °C for 6 hours; E) 220 °C for 3 hours.

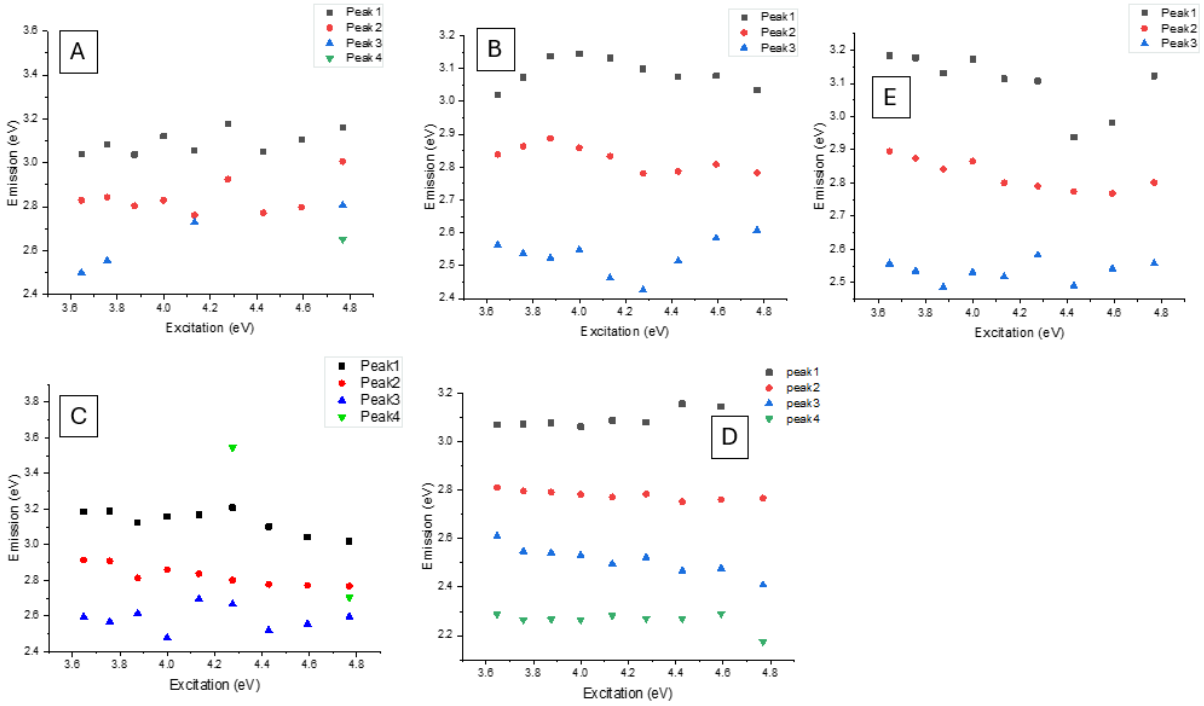

Figure 22: Emission energy of CDs plotted against the excitation energy. A) 180 °C for 3 hours; B) 180 °C for 6 hours; C) 200 °C for 3 hours: D) 200 °C for 6 hours; E) 220 °C for 3 hours.

In Figure 21 A) the CDs exhibit limited fluorescence. The maximum intensity is 40 and it is observed when using higher excitation wavelengths, specifically at 320 nm, 330nm, and 340 nm, with a peak at 400 nm. In Figure 22 A) two discernible peaks are identified, confirmed by the two stable energy bands at 2.8 eV and 3.0 eV. The fluorescence emission is not influenced by excitation wavelengths. However, a third band at 2.6 eV, less well-defined due to the signal noise, shows a possible outlier peak when excited at 260 nm.

As is seen in Figure 21 B), increasing the reaction time to 6 hours shows an improvement in fluorescence emission, with a peak at 400 nm. In Figure 22 B), three stable emission energy bands can be identified at 2.6 eV, 2.8 eV, and 3.0 eV. Again, higher intensities occur with excitation at longer wavelengths (330 nm and 340 nm), but the maximum emission peak is at 260 nm.

As is seen in Figure 21 C), raising the reaction temperature to 200 °C for 3 hours results in CDs with significantly higher fluorescence intensity at 120, with emission peaks at 320, 330, and 340 nm. In Figure 22 C) three stable energy bands are observed at 2.6 eV, 2.8 eV, and 3.2 eV, with two possible outliers when the aqueous solution of CDs is excited at 260 and 290 nm.

As reported in Figure 21 D) is seen that optimal conditions are found to be 200 °C for 6 hours, with a maximum fluorescence intensity at 450 nm when excited at 260 nm. In this case, higher fluorescence is observed at shorter wavelengths (260 and 270 nm), with a decrease between 280 and 300 nm, followed by an increase between 310 and 340 nm. A redshift at 500 nm, related to larger particle sizes, is also noted. In Figure 22 D), four emission energy bands at 2.2 eV, 2.6 eV, 2.8 eV, and 3.1 eV are distinguishable, indicating a fluorescence emission behavior independent of the excitation wavelength.

As is observed in Figure 21 E), at 220 °C for 3 hours, despite increased fluorescence intensity, there is no significant improvement in the fluorescence emission of carbon dots. The peak is stable at 450 nm for excitation wavelengths of 160, 330, and 340 nm, with variations between 270 and 300 nm and an increase between 310 and 340 nm. In Figure 22 D), three wavelength-independent emission bands at 2.5 eV, 2.9 eV, and 3.2 eV are distinguished.

All five synthesized samples exhibit blue fluorescence emission, characterized by a peak at 450 nm and excitation-independent behavior. The sample chosen for cytocompatibility is the one synthesized at 200 °C for 6 hours. It demonstrates one of the highest fluorescence intensities (approximately 100) when excited at 260 nm, and a slightly lower intensity (around 80) when excited at 330 nm and 340 nm. In addition to displaying blue fluorescence emission, a redshift is observed, indicating lower emission energy.

4.1.2 FT-IR Spectroscopy

To investigate the chemical structure of the synthesized CDs, FT-IR analysis was conducted, focusing on the bending, and stretching vibrations of chemical bonds.

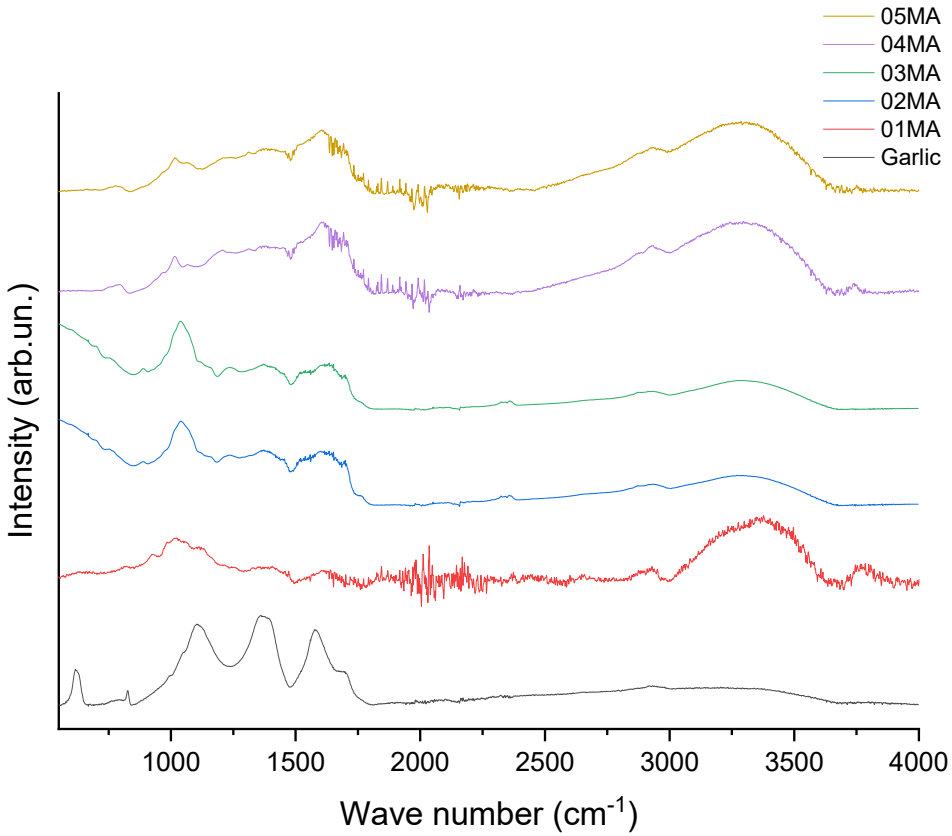

Figure 23: Comparative FT-IR analysis of garlic and different synthesized CDs.

In Figure 23, signal acquisitions related to garlic and synthesized CDs under different time and temperature conditions are presented. The legend denotes each synthesis with specific abbreviations: Garlic stands for freeze-dried garlic, 01MA refers to the sample synthesized at 180 °C for 3 hours, 02MA corresponds to the sample synthesized at 180 °C for 6 hours, 03MA to the sample at 200 °C for 3 hours, 04MA to the sample at 200 °C for 6 hours, and 05MA to the sample at 220 °C for 3 hours.

Before the FT-IR analysis of the CDs, an IR analysis of garlic was carried out for comparative purposes. The resulting graph delineates various regions, each associated with distinct bond vibration modes. In the range between 3000 cm^{-1} and 3600 cm^{-1}, the stretching vibration of OH bonds is highlighted. Vibrations related to saturated CH bonds, characterized by a lower peak compared to OH bonds, are identified between 2800 cm^{-1} and 3000 cm^{-1}. In the region from 1700 cm^{-1} to 2000 cm^{-1}, almost complete absence of stretching associated with the C=O double bond, and hence carboxylics, carbonyls, and amides, is observed. Around 1660 cm^{-1}, a peak related to the C=C double bond emerges, which may indicate the presence of aromatic domains, as well as aliphatic ones. Analysis of this peak allows examination of the temperature effect on the carbohydrate structure, providing insights into whether the aromatization of macromolecules present in the starting biomass has occurred. Lastly, a peak at 1100 cm^{-1} is noted, due to C-O stretching associated with ether functions.

A comparative analysis reveals that during the hydrothermal treatment of garlic to produce CDs, observable changes occur in the shape and intensity of the OH stretching band. This variation is attributed to the oxidation of the material induced by the treatment. Oxidation leads to the formation of carboxyl groups, evidenced by the emergence of structured bands in the region between 1600 cm^{-1} and 1700 cm^{-1}. This phenomenon is associated with dehydration reactions that result in the aromatization of sugars, as described in [56]. Hydrothermal synthesis allows to obtain polymeric CDs with a more aromatized core and an external structure rich in hydroxyl groups. The final structure of the CDs differs from the initial garlic biomass.

This variation prompted the investigation of various temperatures, as temperature is the controlled parameter in hydrothermal synthesis, along with the presence or absence of sulfuric acid, an agent that promotes hydrolysis and carbonization at high temperatures. CDs synthesized at this temperature were chosen as they exhibited the best compromise between yield, fluorescence emission, and degree of carbonization.

4.1.3 Thermogravimetric Analysis

Thermogravimetry is a thermal analysis method in which a sample, placed in an alumina crucible atop a balance, undergoes heating in an inert atmosphere to gather insights into the chemical structure of carbon dots. The temperature increase occurs through a ramp of 10 °C/min, allowing for the quantification of the groups and structures present in the nanoparticles, as specific bonds break at distinct

temperatures. Weight losses obtained from this process provide valuable information on the structure and chemical composition of the carbon dots.

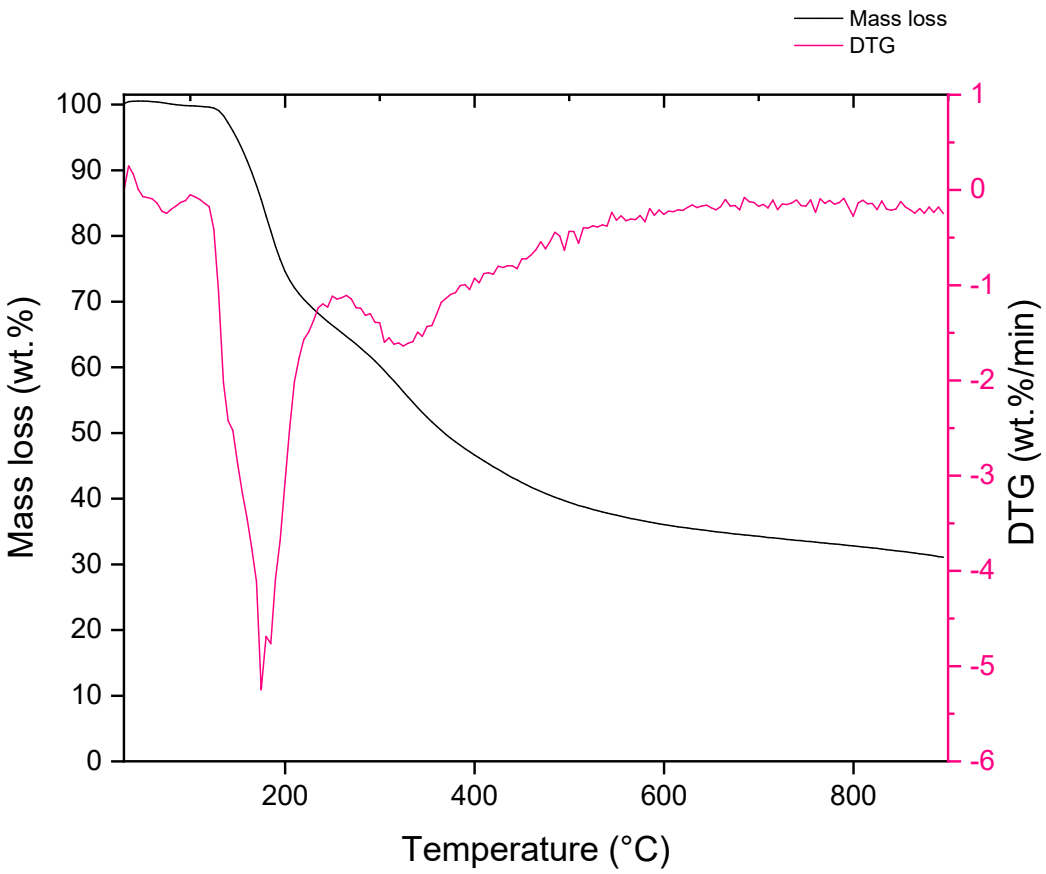

Figure 24: Thermogravimetric analysis of CDs.

As reported in Figure 24, the percentage weight loss of the sample is presented as a function of temperature. Additionally, the first derivative is plotted to facilitate a more detailed analysis of the peaks and temperature degradation intervals. Five decomposition stages can be identified. The first, occurring between 34 °C and 100 °C, exhibits a weight loss of 0.5%, attributed to the evaporation of surface-adsorbed water. In the second decomposition stage, spanning 100 to 168 °C, there is a 5% weight loss due to surface-adsorbed water. The third stage, from 168 °C to 250 °C, presents a 30% weight loss resulting from the degradation of heteroatoms, involving the multiple breakage of bonds and the consequent loss of entire molecules containing heteroatoms such as OH, COOH, C=O, amides, amines, CSH, and CSSC. The fourth stage, extending from 250 °C to 380 °C, indicates an 18% weight loss due to the breaking of C-C bonds. The fifth weight loss, also 18%, occurs when heating from 380 to 900 °C and is associated with the degradation of aromatic species. This is not a fixed decomposition step, as a structured material is degrading. While the shell is broken with a simultaneous and brittle rupture of all functional groups, the core breaks more slowly, as evidenced by the first derivative. The material undergoes a strong carbonization, with rearrangement mechanisms that form carbon.

At 800 °C, the graph begins to plateau as structures become more stable because non-degraded carbon tends to pyrolyze.

4.1.4 UV-Vis Spectroscopy

The foundation of this study revolves around the investigation of the scavenging properties of CDs. This is achieved through the utilization of UV-Vis spectroscopy, focusing on electronic transitions within the samples and evaluating absorption within the visible wavelength range (380-800 nm). Analysis of CDs in a solution with distilled water reveals an increase in absorption associated with elevated synthesis parameters such as temperature and reaction time.

Analyses are conducted using a UV-Vis spectrometer, assessing the degradation of a red dye extracted from cochineal under UV irradiation, both in the absence and presence of CDs. The chosen red dye exhibits structural fragility akin to that of carminic acid (E120), predisposing it to degradation due to easily oxidizable parts (C=O).

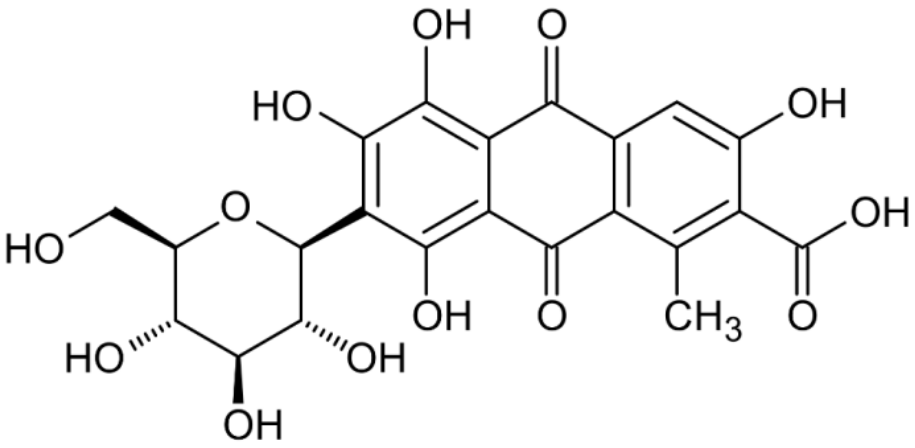

Figure 25: Structure of carminic acid (E120).

Before UV exposure, the construction of a calibration curve is imperative. It is applied Lambert Beer's law for diluted solutions, to calculate the absorbance (A) as a function of the concentration of the sample solution (c) in mg/mL, the optical path length (l) in cm, and the molar extinction coefficient (ε) [159]

$$A = \varepsilon \cdot l \cdot c \qquad (1)$$

Since l = 1 cm, the angular coefficient m of the calibration curve is equal to the molar extinction coefficient ε. The calibration curve (Figure 26) is generated by considering the spectra peaks of four solutions at increasing concentrations (C1, C2, C3, C4), analyzed using the UV-Vis spectrometer. Absorbance peaks are represented as a function of concentrations.

Solution	Concentration (mg/mL)	Peak absorption
C1	0.01000	0.08799
C2	0.00500	0.04489
C3	0.00250	0.02316
C4	0.00125	0.01510

Table 3: Absorption peaks related to water and dye solutions dilute useful for the construction of the calibration line of the non-irradiated dye.

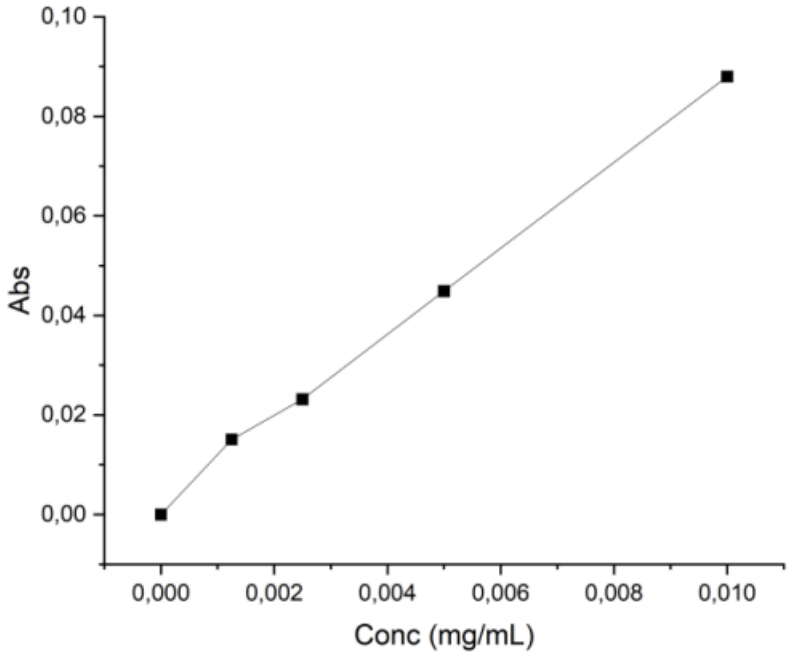

Figure 26: Calibration line of the unirradiated red dye.

The calibration curve facilitates the determination of dye concentration in subsequent analyses. Subsequent UV irradiation experiments will enable the assessment of dye degradation in the presence and absence of CDs, verifying their efficacy as antioxidant agents.

The S1, S2, and S3 solutions were exposed to UV light for 10, 20, and 30 minutes, respectively. Their spectra were compared against the calibration curve of the untreated dye to quantify the reduction in maximum absorption, providing insights into the extent of degradation induced by UV irradiation.

Analysis of the solutions (all at a concentration of 0.01 mg/mL) yielded the following absorption peaks: 0.07988, 0.07382, and 0.06465 for S1, S2, and S3, respectively (refer to Table 4).

Solution	Irradiation time (min)	Peak absorption
S1	10	0.07988
S2	20	0.07382
S3	30	0.06465

Table 4: Values of absorption peaks related to water and dye solutions subjected to UV irradiation for different times useful for the choice of the irradiation causing increased degradation of the red dye.

Opting for a 30-minute irradiation period on the dye samples with CDs was based on the lower peak value of S3, as lower peaks indicate a more significant reduction in absorption with longer irradiation times, indicative of enhanced dye degradation.

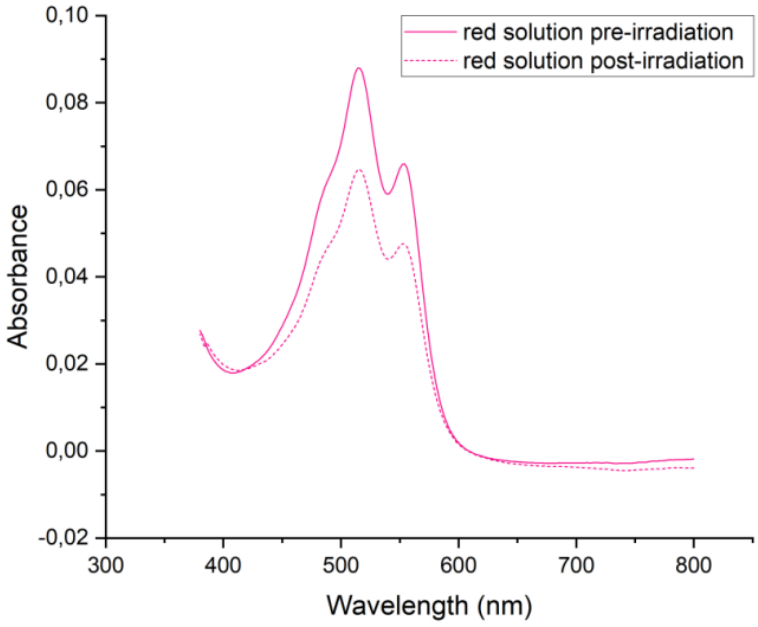

Figure 27: Degradation of red dye cochineal extract after exposure to UV rays for thirty minutes. This dye is more brittle than other types of dyes and is chosen in this thesis work because it serves to carry out a study on preservation employing CDs.

In Figure 27, a reduction in the absorption peak of the dye solution is evident, decreasing from 0.08799 to 0.06465 post-irradiation. The subsequent analysis involves examining samples comprising distilled water and dye with the addition of CDs, both pre-and post-irradiation. The similarity in peaks between the spectra of CDs-irradiated solutions and those of non-irradiated solutions suggests that CDs effectively suppress reactive oxygen species (ROS). The sulfur groups within the CDs react with these species, maintaining the absorption properties of the remaining compound.

Figure 28 reports the UV-Vis spectra pre- and post-irradiation for 30 minutes of the red dye solution combined with each CD sample. It is observed that the absorbance peak remains the same for both the non-irradiated and irradiated solutions for all the solutions tested.

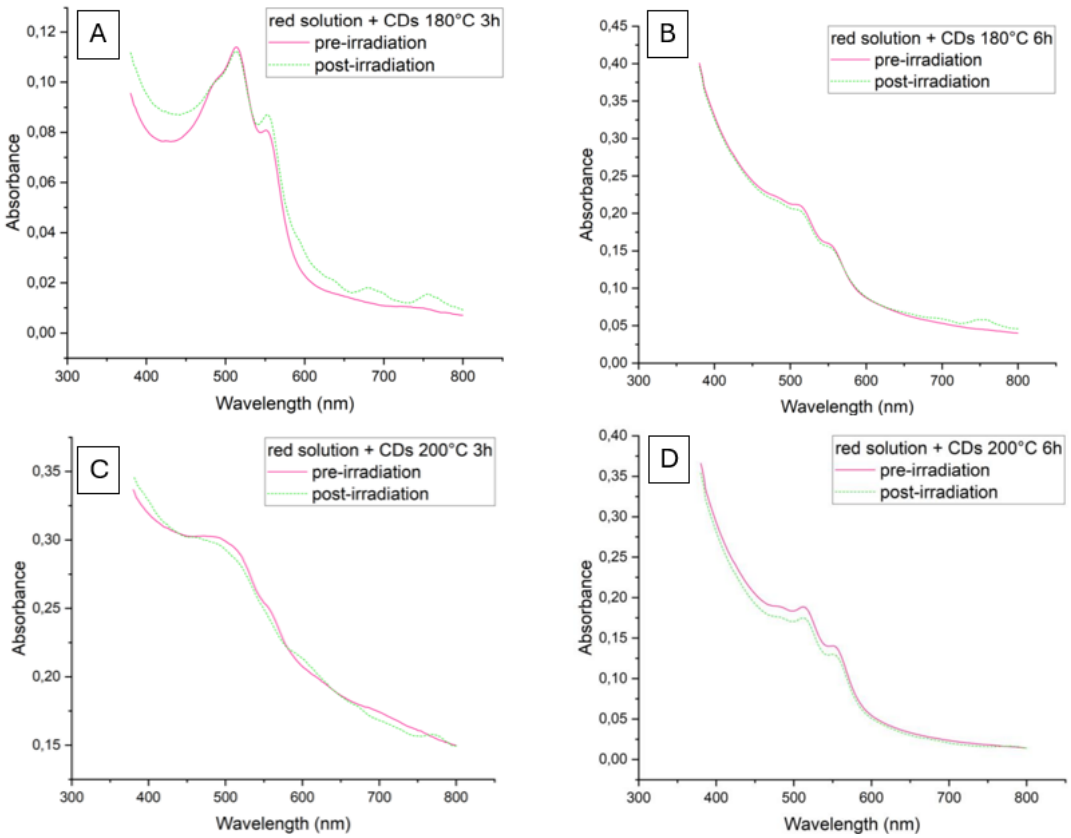

Figure 28: Comparison of UV-Vis pre-irradiation and post-irradiation spectra of solution of red dye combined with CDs synthesized at A)180°C for 3 hours, B) .180°C for 6 hours, C) 200 °C for 3 hours, D) 200 °C for 6 hours.

In Figure 28 A), it is observed that the absorbance peak is 0.12. In Figure 28 B), it can be observed that the absorbance peak rises to approximately 0.2. In Figure 28 C), the absorbance peak registers an increase compared to the preceding two instances, reaching approximately 0.3. In Figure 28 D, the peak once again decreases to approximately 0.2.

The analysis of the sample obtained at 220 °C for three hours has not been conducted. This stems from the clear findings in fluorescence analyses, which indicate that the increase in temperature does not lead to significant improvements in the optical properties of the sample. The lack of substantial enhancements does not justify the additional energy required to raise the process temperature.

4.1.5 Atomic Force Microscopy

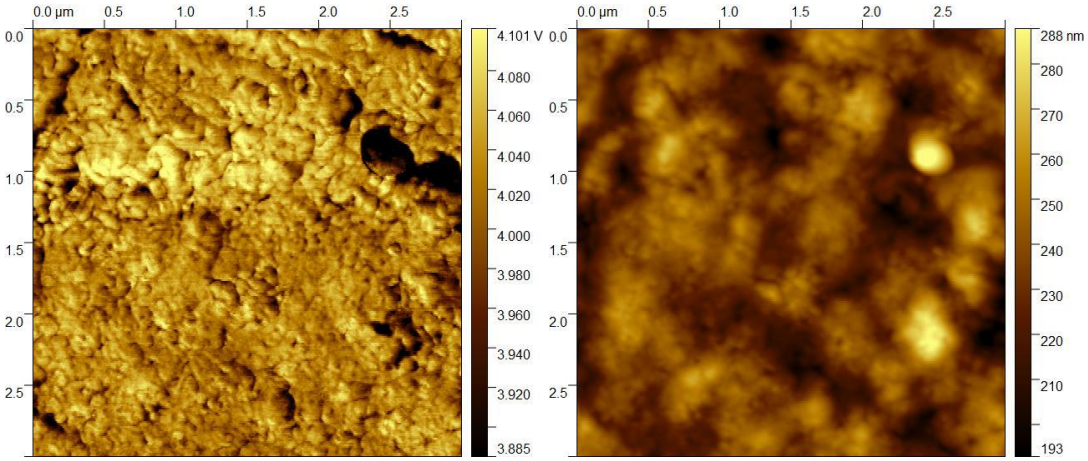

Figure 29: Phase image and surface topography of the CDs are reported respectively.

The AFM technique was employed to gather information regarding the size of CDs and their propensity to form aggregates. Data acquisition was performed at the edge of the deposition droplet. Figure 29 displays both the topography and a phase image, with carbon dots highlighted as the darker regions.

The image size is 3x3 µm, indicating the spatial area represented in the figure. These details provide crucial insights into the morphology and behavior of the nanoparticles under scrutiny through the AFM technique.

From the phase analyses, a histogram (Figure 30) was derived, revealing that the nanoparticles exhibit an average size ranging between 30 and 40 nm. In general, the dimensional range spans from 10 to 80 nm. It is noteworthy that there is a limited tendency for the nanoparticles to aggregate, which could be considered a positive characteristic depending on the research objectives or application.

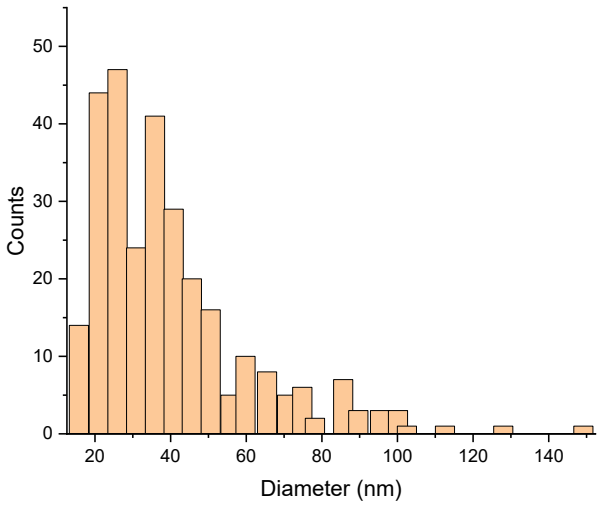

Figure 30: Histogram of CDs' diameter (nm) from phase image.

4.2 MTT assay

To test the cytocompatibility of the synthesized compounds, lung adenocarcinoma cells, i.e. A549-GFP+, were cultured with or without the CDs and their viability was assessed by MTT assay. As shown in Figure 31, CDs treatment did not affect cell behavior. The results were shown as the mean value of optical density +/- standard deviation and not-treated cells were used as control (ctrl). Not-statistically significant differences were detected among the experimental groups, confirming the cytocompatibility of the designed CDs.

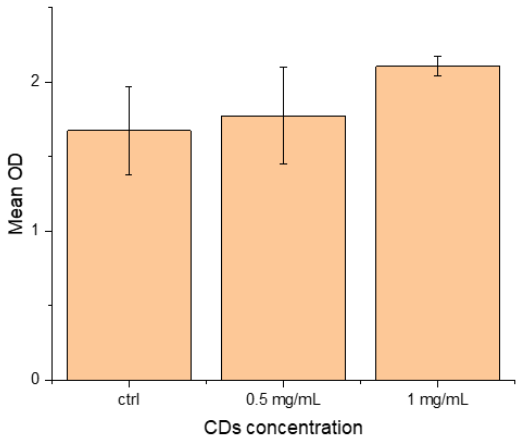

Figure 31: Cellular metabolic activity measured through MTT assay.

In Figure 32 A-D, and in Figure 33 E-G, images show cell morphology before and after the adding of CDs. Importantly, a uniform cell distribution is observed before CDs treatment while, after the adding of a 0.5 mg/mL CDs solution (Figure 30 C), small CD aggregates emerge as black dots, indicating incomplete homogenization post-sonication. These small aggregates disperse well initially, but after 24

hours (Figure 32 D), there is a tendency for increased aggregation, possibly influenced by interactions with proteins in the culture medium.

At a concentration of 1 mg/mL, a more noticeable increase in aggregates is observed compared to 0.5 mg/mL, especially after 24 hours (Figure 33 F-G). Results indicates viable cells beneath the CD aggregates, suggesting that CDs can be floating within the culture medium.

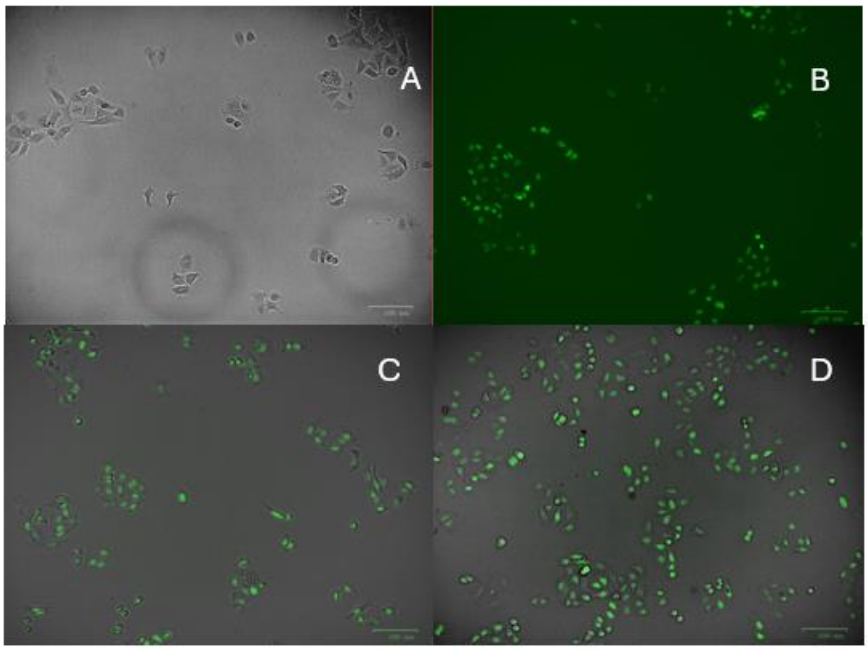

Figure 32: ZOE images of A549-GFP cells2. A) Brightfield acquisition of control sample. B) Greenfield acquisition of control sample. C) Merged (BF and GF) ZOE image of cells treated at 0.5 mg/mL. D) Merged (BF and GF) ZOE image of cells treated at 1 mg/mL.

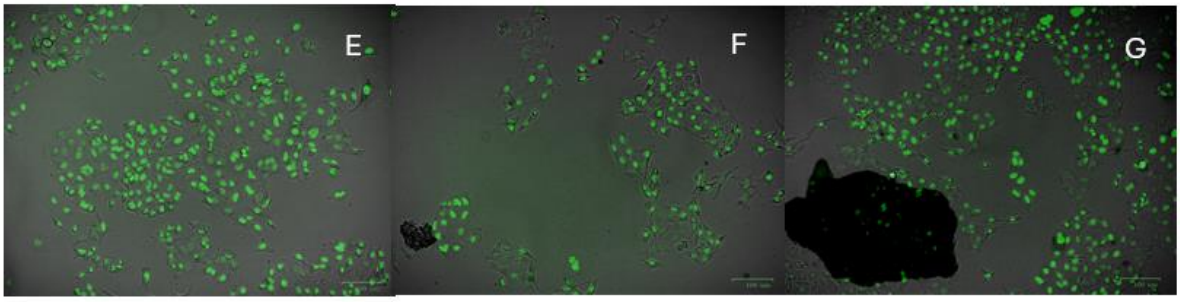

Figure 33: Merged (BF and GF) ZOE images after 24 hours of E) control group; F) cells treated at 0.5 mg/mL; G) cells treated at 1 mg/mL.

To validate the fluorescence of the CDs, an acquisition in the Bluefield was conducted, revealing no detectable fluorescence, contrary to fluorescence spectroscopy results. However, a substantial background fluorescence is present. Nevertheless, the CD aggregates are visible, although non-fluorescent. Two potential explanations can be considered. One explanation involves an interaction between the proteins within the culture medium and the CDs, resulting in fluorescence quenching. Alternatively, the reduction in emitted fluorescence intensity could be attributed to the formation of CD

aggregates, induced by interactions with proteins dissolved in the medium. This reduction occurs as nanoparticle size increases, leading to a decrease in the HOMO-LUMO band gap.

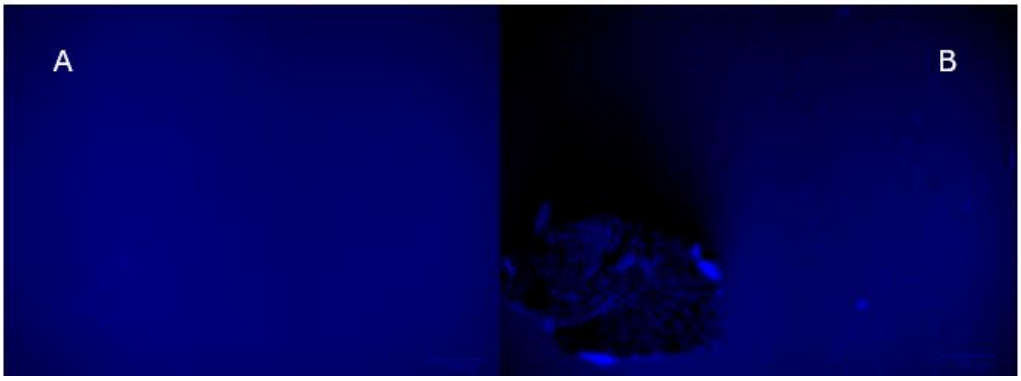

Figure 34: A) Bluefield of cells treated with 0.5 mg/mL of CDs. B) Bluefield of cells treated with 1 mg/mL of CDs

5 Conclusions

The production of garlic-based CDs represents an intriguing approach leveraging the properties of natural biomass to obtain advanced nanomaterials. This methodology proves especially attractive for specific applications, particularly when harnessing the unique properties of garlic in the resulting nanomaterials. Throughout this thesis, CDs were synthesized using a hydrothermal synthesis method, with garlic as the starting biomass. Five syntheses were conducted under different time and temperature conditions (180°C-220°C, for 3-6 hours), followed by various characterizations.

Fluorimeter analysis revealed the ability of these nanoparticles to emit blue fluorescence. However, this fluorescence was not confirmed by cell analyses using the Bluefield fluorescence microscope, where CDs did not exhibit fluorescence. Dimensional analysis indicated CDs with average sizes ranging from 20-40 nm, with a limited tendency to form aggregates. Nevertheless, cellular tests revealed incomplete homogenization and solubilization of CDs, with a propensity for aggregate formation.

It is important to underline that cellular tests are still in the preliminary stage and require optimization of the materials and methods employed to achieve proper solubilization of CDs in the culture medium.

Chemical composition analyses highlighted the preservation of garlic's structure, identifying the presence of numerous sulphur-containing functional groups. CDs manifested a core-shell structure with the same functional groups but at different concentrations. TGA indicated a predominance of carboxylic groups on the surface and hydroxyl groups in the core.

The conducted analyses demonstrated the effective ability of CDs to act as radical scavengers *in vitro*, suggesting potential use in reducing oxidative stress in cells. MTT assays indicated well-preserved cellular viability after 24 hours of incubation with CDs at concentrations of 0.5 mg/mL and 1 mg/mL.

These findings suggest that the synthesized CDs possess promising capabilities, hinting at their potential application in the biomedical field. Thanks to their ability to generate and absorb ROS, CDs can be exploited as both antibacterial and antioxidant agents. Further analyses and bioassays are necessary to assess the translational potential of these materials in a clinical setting, potentially for treating oxidative stress in neuronal cells or as theranostic agents. The use of a starting biomass like garlic contributes to making the production process sustainable, aligning with a circular economy approach through the recycling of waste substances. The intrinsic properties of garlic, combined with those of CDs, make these nanomaterials suitable for advanced biomedical applications.

Acknowledgments

In conclusion of this work, I wish to acknowledge the contribution of all the individuals who, with their constant support, have made the completion of this thesis possible. Without them, this work would not have been possible, and it would be more difficult.

I wish to express my deep gratitude to my supervisor, Professor Tagliaferro, who, thanks to his knowledge, expertise, and experience, has been a constant source of inspiration for me. I would also like to extend my thanks to my co-supervisor, Professor Frascella, for giving me the opportunity to delve into a fascinating and fundamental aspect for my thesis. A sincere thank you goes to my co-supervisor, Professor Bartoli, who has supported, guided, and helped me through every phase of writing this work since day one. His presence and support have been a constant for me. Capable of seeing people beyond numbers, he has always believed in my potential. I also thank ProfessorPiatti, who kindly and generously assisted me during one of the characterizations carried out during this thesis.

Bibliography

1. Kumar, H., et al., *Metallic nanoparticle: a review.* Biomed. J. Sci. Tech. Res, 2018. **4**(2): p. 3765-3775.
2. C Thomas, S., P. Kumar Mishra, and S. Talegaonkar, *Ceramic nanoparticles: fabrication methods and applications in drug delivery.* Current pharmaceutical design, 2015. **21**(42): p. 6165-6188.
3. Chen, W., J.Z. Zhang, and A.G. Joly, *Optical properties and potential applications of doped semiconductor nanoparticles.* Journal of nanoscience and nanotechnology, 2004. **4**(8): p. 919-947.
4. Joudeh, N. and D. Linke, *Nanoparticle classification, physicochemical properties, characterization, and applications: a comprehensive review for biologists.* Journal of Nanobiotechnology, 2022. **20**(1): p. 262.
5. Toshima, N. and T. Yonezawa, *Bimetallic nanoparticles—novel materials for chemical and physical applications.* New Journal of Chemistry, 1998. **22**(11): p. 1179-1201.
6. Nascimento, M.A., et al., *Synthesis of polymetallic nanoparticles from spent lithium-ion batteries and application in the removal of reactive blue 4 dye.* Journal of Cleaner Production, 2018. **202**: p. 264-272.
7. Khan, I., K. Saeed, and I. Khan, *Nanoparticles: Properties, applications and toxicities.* Arabian journal of chemistry, 2019. **12**(7): p. 908-931.
8. Giljohann, D.A., et al., *Gold nanoparticles for biology and medicine.* Spherical Nucleic Acids, 2020: p. 55-90.
9. Abe, S., et al. *Internal distribution of micro-/nano-sized inorganic particles and their cytocompatibility*. in *IOP Conference Series: Materials Science and Engineering*. 2011. IOP Publishing.
10. Hosono, T., et al., *Synthesis of magnetite nanoparticles for AC magnetic heating.* Journal of Magnetism and Magnetic Materials, 2009. **321**(19): p. 3019-3023.
11. Wilhelm, C., J.-P. Fortin, and F. Gazeau, *Tumour cell toxicity of intracellular hyperthermia mediated by magnetic nanoparticles.* Journal of nanoscience and nanotechnology, 2007. **7**(8): p. 2933-2937.
12. Karlsson, H.L., et al., *Size-dependent toxicity of metal oxide particles—a comparison between nano-and micrometer size.* Toxicology letters, 2009. **188**(2): p. 112-118.
13. Khan, S.S., A. Mukherjee, and N. Chandrasekaran, *Studies on interaction of colloidal silver nanoparticles (SNPs) with five different bacterial species.* Colloids and Surfaces B: Biointerfaces, 2011. **87**(1): p. 129-138.
14. Singh, S.P., et al., *Silver nanoparticles: Biomedical applications, toxicity, and safety issues.* Int. J. Res. Pharm. Pharm. Sci, 2017. **4**(2): p. 1-10.
15. De Matteis, V., *Exposure to inorganic nanoparticles: routes of entry, immune response, biodistribution and in vitro/in vivo toxicity evaluation.* Toxics, 2017. **5**(4): p. 29.
16. Tamarov, K., et al., *Approaches to improve the biocompatibility and systemic circulation of inorganic porous nanoparticles.* Journal of Materials Chemistry B, 2018. **6**(22): p. 3632-3649.
17. Estrada, L.H. and J. Champion, *Protein nanoparticles for therapeutic protein delivery.* Biomaterials science, 2015. **3**(6): p. 787-799.
18. Verma, M.L., et al., *Carbohydrate and protein based biopolymeric nanoparticles: current status and biotechnological applications.* International journal of biological macromolecules, 2020. **154**: p. 390-412.
19. Marradi, M., I. García, and S. Penadés, *Carbohydrate-based nanoparticles for potential applications in medicine.* Progress in molecular biology and translational science, 2011. **104**: p. 141-173.
20. Lingayat, V.J., N.S. Zarekar, and R.S. Shendge, *Solid lipid nanoparticles: a review.* Nanosci. Nanotechnol. Res, 2017. **4**(2): p. 67-72.
21. Lu, X.-Y., et al., *Polymer nanoparticles.* Progress in molecular biology and translational science, 2011. **104**: p. 299-323.
22. Kumar, V., G. Toffoli, and F. Rizzolio, *Fluorescent carbon nanoparticles in medicine for cancer therapy*. 2013, ACS Publications. p. 1012-1013.

23. Bharali, D.J., et al., *Nanoparticles and cancer therapy: a concise review with emphasis on dendrimers.* International journal of nanomedicine, 2009: p. 1-7.
24. Panahi, Y., et al., *Recent advances on liposomal nanoparticles: synthesis, characterization and biomedical applications.* Artificial cells, nanomedicine, and biotechnology, 2017. **45**(4): p. 788-799.
25. Tyrrell, Z.L., Y. Shen, and M. Radosz, *Fabrication of micellar nanoparticles for drug delivery through the self-assembly of block copolymers.* Progress in Polymer Science, 2010. **35**(9): p. 1128-1143.
26. Solans, C., et al., *Nano-emulsions.* Current opinion in colloid & interface science, 2005. **10**(3-4): p. 102-110.
27. Yallapu, M.M., M. Jaggi, and S.C. Chauhan, *Design and engineering of nanogels for cancer treatment.* Drug discovery today, 2011. **16**(9-10): p. 457-463.
28. Rodrigues, M.Q., P.M. Alves, and A. Roldão, *Functionalizing ferritin nanoparticles for vaccine development.* Pharmaceutics, 2021. **13**(10): p. 1621.
29. Wang, Y. and A. Hu, *Carbon quantum dots: synthesis, properties and applications.* Journal of Materials Chemistry C, 2014. **2**(34): p. 6921-6939.
30. Wang, L., et al., *Exploring and analyzing the systemic delivery barriers for nanoparticles.* Advanced Functional Materials, 2024. **34**(8): p. 2308446.
31. Sadeghi, S., et al., *Oral administration of protein nanoparticles: An emerging route to disease treatment.* Pharmacological research, 2020. **158**: p. 104685.
32. Dickinson, P.A., S.W. Howells, and I.W. Kellaway, *Novel nanoparticles for pulmonary drug administration.* Journal of drug targeting, 2001. **9**(4): p. 295-302.
33. de Almeida, M.S., et al., *Understanding nanoparticle endocytosis to improve targeting strategies in nanomedicine.* Chemical society reviews, 2021. **50**(9): p. 5397-5434.
34. Strojny, B., et al., *Long term influence of carbon nanoparticles on health and liver status in rats.* PloS one, 2015. **10**(12): p. e0144821.
35. Liu, J., R. Li, and B. Yang, *Carbon dots: A new type of carbon-based nanomaterial with wide applications.* ACS Central Science, 2020. **6**(12): p. 2179-2195.
36. Xia, C., et al., *Evolution and synthesis of carbon dots: from carbon dots to carbonized polymer dots.* Advanced Science, 2019. **6**(23): p. 1901316.
37. Giordano, M.G., et al., *An overview on carbon quantum dots optical and chemical features.* Molecules, 2023. **28**(6): p. 2772.
38. Xu, X., et al., *Electrophoretic analysis and purification of fluorescent single-walled carbon nanotube fragments.* Journal of the American Chemical Society, 2004. **126**(40): p. 12736-12737.
39. Sun, Y.-P., et al., *Quantum-sized carbon dots for bright and colorful photoluminescence.* Journal of the American Chemical Society, 2006. **128**(24): p. 7756-7757.
40. Li, S., et al., *The development of carbon dots: From the perspective of materials chemistry.* Materials Today, 2021. **51**: p. 188-207.
41. Jing, H.H., et al., *Green carbon dots: Synthesis, characterization, properties and biomedical applications.* Journal of Functional Biomaterials, 2023. **14**(1): p. 27.
42. Shi, W., et al., *Synthesis mechanisms, structural models, and photothermal therapy applications of top-down carbon dots from carbon powder, graphite, graphene, and carbon nanotubes.* International journal of molecular sciences, 2022. **23**(3): p. 1456.
43. Li, F., D. Yang, and H. Xu, *Non-metal-heteroatom-doped carbon dots: synthesis and properties.* Chemistry–A European Journal, 2019. **25**(5): p. 1165-1176.
44. Barman, M.K. and A. Patra, *Current status and prospects on chemical structure driven photoluminescence behaviour of carbon dots.* Journal of Photochemistry and Photobiology C: Photochemistry Reviews, 2018. **37**: p. 1-22.
45. Yan, F., et al., *The fluorescence mechanism of carbon dots, and methods for tuning their emission color: A review.* Microchimica Acta, 2019. **186**: p. 1-37.
46. Medeiros, G.A., et al., *Carbon dots (C-dots): fluorescence processes and bioimaging*, in *Quantum Materials, Devices, and Applications*. 2023, Elsevier. p. 201-213.
47. Zhang, B., et al., *Assignment of Core and Surface States in Multicolor-Emissive Carbon Dots.* Small, 2023. **19**(31): p. 2204158.

48. Yoo, H.J. and B.E. Kwak, *Competition of the roles of π-conjugated domain between emission center and quenching origin in the photoluminescence of carbon dots depending on the interparticle separation.* Carbon, 2021. **183**: p. 560-570.
49. Tang, L., et al., *Deep ultraviolet photoluminescence of water-soluble self-passivated graphene quantum dots.* ACS nano, 2012. **6**(6): p. 5102-5110.
50. Mandal, B., S. Sarkar, and P. Sarkar, *Exploring the electronic structure of graphene quantum dots.* Journal of Nanoparticle Research, 2012. **14**: p. 1-8.
51. Yan, X., et al., *Independent tuning of the band gap and redox potential of graphene quantum dots.* The journal of physical chemistry letters, 2011. **2**(10): p. 1119-1124.
52. Mintz, K.J., et al., *A deep investigation into the structure of carbon dots.* Carbon, 2021. **173**: p. 433-447.
53. Yan, X., et al., *Large, solution-processable graphene quantum dots as light absorbers for photovoltaics.* Nano letters, 2010. **10**(5): p. 1869-1873.
54. Yan, X., X. Cui, and L.-s. Li, *Synthesis of large, stable colloidal graphene quantum dots with tunable size.* Journal of the American Chemical Society, 2010. **132**(17): p. 5944-5945.
55. Yuan, F., et al., *Bright multicolor bandgap fluorescent carbon quantum dots for electroluminescent light-emitting diodes.* Advanced materials, 2017. **29**(3): p. 1604436.
56. Seven, E.S., et al., *Hydrothermal vs microwave nanoarchitechtonics of carbon dots significantly affects the structure, physicochemical properties, and anti-cancer activity against a specific neuroblastoma cell line.* Journal of colloid and interface science, 2023. **630**: p. 306-321.
57. Hai, X., et al., *An acid-free microwave approach to prepare highly luminescent boron-doped graphene quantum dots for cell imaging.* Journal of Materials Chemistry B, 2015. **3**(47): p. 9109-9114.
58. Liu, H., et al., *Synthesis and biomedical applications of graphitic carbon nitride quantum dots.* Journal of Materials Chemistry B, 2019. **7**(36): p. 5432-5448.
59. Liyanage, P.Y., et al., *Carbon nitride dots: a selective bioimaging nanomaterial.* Bioconjugate chemistry, 2018. **30**(1): p. 111-123.
60. Cilingir, E.K., et al., *Surface modification of carbon nitride dots by nanoarchitectonics for better drug loading and higher cancer selectivity.* Nanoscale, 2022. **14**(27): p. 9686-9701.
61. Wiśniewski, M., *The Consequences of Water Interactions with Nitrogen-Containing Carbonaceous Quantum Dots—The Mechanistic Studies.* International Journal of Molecular Sciences, 2022. **23**(22): p. 14292.
62. Zhou, Y., et al., *Polymers in carbon dots: a review.* Polymers, 2017. **9**(2): p. 67.
63. Liu, H., et al., *A review of carbon dots in synthesis strategy.* Coordination Chemistry Reviews, 2024. **498**: p. 215468.
64. Arora, N. and N. Sharma, *Arc discharge synthesis of carbon nanotubes: Comprehensive review.* Diamond and related materials, 2014. **50**: p. 135-150.
65. Zhu, J., et al., *Chemical Oxidation Synthesized High-yield Carbon Dots for Acid Corrosion Inhibition of Q235 Steel.* ChemistrySelect, 2023. **8**(7): p. e202204621.
66. An, Q., et al., *Electrochemical synthesis of carbon dots with a Stokes shift of 309 nm for sensing of Fe3+ and ascorbic acid.* Dyes and Pigments, 2021. **185**: p. 108878.
67. Ming, H., et al., *Large scale electrochemical synthesis of high quality carbon nanodots and their photocatalytic property.* Dalton transactions, 2012. **41**(31): p. 9526-9531.
68. Otten, M., et al., *Pyrolysis and solvothermal synthesis for carbon dots: role of purification and molecular fluorophores.* Langmuir, 2022. **38**(19): p. 6148-6157.
69. Kang, Z. and S.-T. Lee, *Carbon dots: advances in nanocarbon applications.* Nanoscale, 2019. **11**(41): p. 19214-19224.
70. Choi, Y., et al., *Carbon dots: bottom-up syntheses, properties, and light-harvesting applications.* Chemistry–An Asian Journal, 2018. **13**(6): p. 586-598.
71. de Medeiros, T.V., et al., *Microwave-assisted synthesis of carbon dots and their applications.* Journal of Materials Chemistry C, 2019. **7**(24): p. 7175-7195.
72. Han, Z., et al., *Hydrothermal synthesis of carbon dots and their application for detection of chlorogenic acid.* Luminescence, 2020. **35**(7): p. 989-997.
73. Ye, Z., et al., *One-step and one-precursor hydrothermal synthesis of carbon dots with superior antibacterial activity.* ACS Applied Bio Materials, 2020. **3**(10): p. 7095-7102.

74. Zhao, P., et al., *One-step solvothermal synthesis of high-emissive amphiphilic carbon dots via rigidity derivation.* Chemical Science, 2018. **9**(5): p. 1323-1329.
75. Finlayson, L., et al., *Depth penetration of light into skin as a function of wavelength from 200 to 1000 nm.* Photochemistry and Photobiology, 2022. **98**(4): p. 974-981.
76. Sharma, A. and J. Das, *Small molecules derived carbon dots: synthesis and applications in sensing, catalysis, imaging, and biomedicine.* Journal of nanobiotechnology, 2019. **17**(1): p. 1-24.
77. Zhou, L., et al., *Carbon nanodots as fluorescence probes for rapid, sensitive, and label-free detection of Hg 2+ and biothiols in complex matrices.* Chemical communications, 2012. **48**(8): p. 1147-1149.
78. Das, R.K., et al., *N-doped carbon quantum dot (NCQD)-Deposited carbon capsules for synergistic fluorescence imaging and photothermal therapy of oral cancer.* Langmuir, 2019. **35**(47): p. 15320-15329.
79. Zhi, D., et al., *Photothermal therapy.* Journal of Controlled Release, 2020. **325**: p. 52-71.
80. Ge, J., et al., *Red-emissive carbon dots for fluorescent, photoacoustic, and thermal theranostics in living mice.* Advanced Materials, 2015. **27**(28): p. 4169-4177.
81. Innocenzi, P. and L. Stagi, *Carbon dots as oxidant-antioxidant nanomaterials, understanding the structure-properties relationship. A critical review.* Nano Today, 2023. **50**: p. 101837.
82. Karagianni, A., et al., *Application of carbon-based quantum dots in photodynamic therapy.* Carbon, 2023. **203**: p. 273-310.
83. Podder, S., et al., *Light-responsive nanomaterials with pro-oxidant and anti-oxidant activity.* Emergent Materials, 2022. **5**(2): p. 455-475.
84. Lim, S.Y., W. Shen, and Z. Gao, *Carbon quantum dots and their applications.* Chemical Society Reviews, 2015. **44**(1): p. 362-381.
85. Liu, Z., et al., *Carbon-quantum-dots-loaded mesoporous silica nanocarriers with pH-switchable zwitterionic surface and enzyme-responsive pore-cap for targeted imaging and drug delivery to tumor.* Advanced healthcare materials, 2016. **5**(12): p. 1401-1407.
86. Singh, I., et al., *Carbon quantum dots: Synthesis, characterization and biomedical applications.* Turk. J. Pharm. Sci, 2018. **15**(2): p. 219-30.
87. Ding, H., et al., *DNA–carbon dots function as fluorescent vehicles for drug delivery.* ACS applied materials & interfaces, 2015. **7**(12): p. 6889-6897.
88. Zheng, M., et al., *Self-targeting fluorescent carbon dots for diagnosis of brain cancer cells.* ACS nano, 2015. **9**(11): p. 11455-11461.
89. Singh, V., et al., *Nitrogen doped carbon quantum dots demonstrate no toxicity under in vitro conditions in a cervical cell line and in vivo in Swiss albino mice.* Toxicology Research, 2019. **8**(3): p. 395-406.
90. Farshbaf, M., et al., *Carbon quantum dots: recent progresses on synthesis, surface modification and applications.* Artificial cells, nanomedicine, and biotechnology, 2018. **46**(7): p. 1331-1348.
91. Begley, C.G. and L.M. Ellis, *Raise standards for preclinical cancer research.* Nature, 2012. **483**(7391): p. 531-533.
92. Braakhuis, H.M., et al., *Progress and future of in vitro models to study translocation of nanoparticles.* Archives of toxicology, 2015. **89**: p. 1469-1495.
93. Zhou, N., et al., *Elucidating the endocytosis, intracellular trafficking, and exocytosis of carbon dots in neural cells.* RSC Advances, 2014. **4**(107): p. 62086-62095.
94. Mavroidi, B., et al., *Carbon Dots–Biomembrane Interactions and Their Implications for Cellular Drug Delivery.* Pharmaceuticals, 2023. **16**(6): p. 833.
95. Cao, L., et al., *Carbon dots for multiphoton bioimaging.* Journal of the American Chemical Society, 2007. **129**(37): p. 11318-11319.
96. Ray, S., et al., *Fluorescent carbon nanoparticles: synthesis, characterization, and bioimaging application.* The Journal of Physical Chemistry C, 2009. **113**(43): p. 18546-18551.
97. Goh, E.J., et al., *Bioimaging of hyaluronic acid derivatives using nanosized carbon dots.* Biomacromolecules, 2012. **13**(8): p. 2554-2561.
98. Liu, C., et al., *Nano-carrier for gene delivery and bioimaging based on carbon dots with PEI-passivation enhanced fluorescence.* Biomaterials, 2012. **33**(13): p. 3604-3613.
99. Rajendran, P., et al., *Antioxidants and human diseases.* Clinica chimica acta, 2014. **436**: p. 332-347.

100. Doreswamy, K., et al., *Nickel-induced oxidative stress in testis of mice: evidence of DNA damage and genotoxic effects.* Journal of andrology, 2004. **25**(6): p. 996-1003.
101. Tepe, B., et al., *In vitro antioxidant activities of the methanol extracts of five Allium species from Turkey.* Food chemistry, 2005. **92**(1): p. 89-92.
102. Khalid, N., S.A. Fawad, and I. Ahmed, *Antimicrobial activity, phytochemical profile and trace minerals of black mulberry (Morus nigra L.) fresh juice.* Pak. J. Bot, 2011. **43**(6): p. 91-96.
103. Nicastro, H.L., S.A. Ross, and J.A. Milner, *Garlic and onions: their cancer prevention properties.* Cancer prevention research, 2015. **8**(3): p. 181-189.
104. Liu, C., et al., *Determination of antioxidant activity in garlic (Allium sativum) extracts subjected to boiling process in vitro.* Journal of Food and Nutrition Research, 2014. **2**(7): p. 383-387.
105. Butt, M.S., et al., *Garlic: nature's protection against physiological threats.* Critical reviews in food science and nutrition, 2009. **49**(6): p. 538-551.
106. Choudhary, R., *Benificial effect of Allium sativum and Allium tuberosum on experimental hyperlipidemia and atherosclerosis.* Pakistan Journal of Physiology, 2008. **4**(2): p. 7-10.
107. Touloupakis, E. and D.F. Ghanotakis, *Nutraceutical use of garlic sulfur-containing compounds*, in *Bio-Farms for Nutraceuticals: Functional Food and Safety Control by Biosensors*. 2010, Springer. p. 110-121.
108. Borek, C., *Antioxidant health effects of aged garlic extract.* The Journal of nutrition, 2001. **131**(3): p. 1010S-1015S.
109. Jikihara, H., et al., *Aged garlic extract inhibits 1, 2-dimethylhydrazine-induced colon tumor development by suppressing cell proliferation.* Oncology reports, 2015. **33**(3): p. 1131-1140.
110. Wu, Z.-R., et al., *Two cinnamoyloctopamine antioxidants from garlic skin attenuates oxidative stress and liver pathology in rats with non-alcoholic steatohepatitis.* Phytomedicine, 2015. **22**(1): p. 178-182.
111. Fasolino, I., et al., *Orally administered allyl sulfides from garlic ameliorate murine colitis.* Molecular nutrition & food research, 2015. **59**(3): p. 434-442.
112. Zhang, X., et al., *Allicin induces apoptosis of the MGC-803 human gastric carcinoma cell line through the p38 mitogen-activated protein kinase/caspase-3 signaling pathway.* Molecular medicine reports, 2015. **11**(4): p. 2755-2760.
113. Bagul, M., S. Kakumanu, and T.A. Wilson, *Crude garlic extract inhibits cell proliferation and induces cell cycle arrest and apoptosis of cancer cells in vitro.* Journal of medicinal food, 2015. **18**(7): p. 731-737.
114. Wang, H.P., et al., *Effect of garlic on blood pressure: A meta-analysis.* The Journal of Clinical Hypertension, 2015. **17**(3): p. 223-231.
115. Mroz, P., et al., *Photodynamic therapy with fullerenes.* Photochemical & Photobiological Sciences, 2007. **6**(11): p. 1139-1149.
116. Stasheuski, A.S., et al., *Photophysical properties and singlet oxygen generation efficiencies of water-soluble fullerene nanoparticles.* Photochemistry and photobiology, 2014. **90**(5): p. 997-1003.
117. Adeleye, A.S., et al., *Photoreactivity of graphene oxide in aqueous system: Reactive oxygen species formation and bisphenol A degradation.* Chemosphere, 2018. **195**: p. 344-350.
118. Hsieh, H.-S. and R.G. Zepp, *Reactivity of graphene oxide with reactive oxygen species (hydroxyl radical, singlet oxygen, and superoxide anion).* Environmental Science: Nano, 2019. **6**(12): p. 3734-3744.
119. Tamtaji, M., et al., *Singlet oxygen photosensitization using graphene-based structures and immobilized dyes: A review.* ACS Applied Nano Materials, 2021. **4**(8): p. 7563-7586.
120. Zhu, Z., et al., *Regulation of singlet oxygen generation using single-walled carbon nanotubes.* Journal of the American Chemical Society, 2008. **130**(33): p. 10856-10857.
121. Ge, J., et al., *A graphene quantum dot photodynamic therapy agent with high singlet oxygen generation.* Nature communications, 2014. **5**(1): p. 4596.
122. Li, X., et al., *Supramolecular phthalocyanine assemblies for improved photoacoustic imaging and photothermal therapy.* Angewandte Chemie, 2020. **132**(22): p. 8708-8712.
123. Nie, X., et al., *Carbon quantum dots: A bright future as photosensitizers for in vitro antibacterial photodynamic inactivation.* Journal of Photochemistry and Photobiology B: Biology, 2020. **206**: p. 111864.

124. Wu, S., et al., *Highly efficient oxygen photosensitization of carbon dots: the role of nitrogen doping.* Nanoscale, 2020. **12**(9): p. 5543-5553.
125. Sun, H., et al., *Deciphering a nanocarbon-based artificial peroxidase: chemical identification of the catalytically active and substrate-binding sites on graphene quantum dots.* Angewandte Chemie International Edition, 2015. **54**(24): p. 7176-7180.
126. Zhou, Y., et al., *How functional groups influence the ROS generation and cytotoxicity of graphene quantum dots.* Chemical communications, 2017. **53**(76): p. 10588-10591.
127. Liu, Y.-Y., et al., *Photodegradation of carbon dots cause cytotoxicity.* Nature communications, 2021. **12**(1): p. 812.
128. Wang, L., et al., *Chlorine-doped graphene quantum dots with enhanced anti-and pro-oxidant properties.* ACS applied materials & interfaces, 2019. **11**(24): p. 21822-21829.
129. Hasanuzzaman, M., et al., *Reactive oxygen species and antioxidant defense in plants under abiotic stress: Revisiting the crucial role of a universal defense regulator.* Antioxidants, 2020. **9**(8): p. 681.
130. Zhang, Q., et al., *A superoxide dismutase/catalase mimetic nanomedicine for targeted therapy of inflammatory bowel disease.* Biomaterials, 2016. **105**: p. 206-221.
131. Zhu, X., et al., *Ru@ CeO2 yolk shell nanozymes: Oxygen supply in situ enhanced dual chemotherapy combined with photothermal therapy for orthotopic/subcutaneous colorectal cancer.* Biomaterials, 2020. **242**: p. 119923.
132. Gao, L., et al., *Intrinsic peroxidase-like activity of ferromagnetic nanoparticles.* Nature nanotechnology, 2007. **2**(9): p. 577-583.
133. Asada, K., *Ascorbate peroxidase–a hydrogen peroxide-scavenging enzyme in plants.* Physiologia plantarum, 1992. **85**(2): p. 235-241.
134. Chen, T., et al., *Natural polyphenol–vanadium oxide nanozymes for synergistic chemodynamic/photothermal therapy.* Chemistry–A European Journal, 2020. **26**(66): p. 15159-15169.
135. Wang, H., et al., *Phenol-like group functionalized graphene quantum dots structurally mimicking natural antioxidants for highly efficient acute kidney injury treatment.* Chemical science, 2020. **11**(47): p. 12721-12730.
136. Zhang, R.-q., et al., *Antioxidative effect of luteolin pretreatment on simulated ischemia/reperfusion injury in cardiomyocyte and perfused rat heart.* Chinese journal of integrative medicine, 2017. **23**: p. 518-527.
137. Arrigoni, O. and M.C. De Tullio, *Ascorbic acid: much more than just an antioxidant.* Biochimica et Biophysica Acta (BBA)-General Subjects, 2002. **1569**(1-3): p. 1-9.
138. Gęgotek, A. and E. Skrzydlewska, *Ascorbic acid as antioxidant.* Vitamins and Hormones, 2023. **121**: p. 247-270.
139. Haida, Z. and M. Hakiman, *A comprehensive review on the determination of enzymatic assay and nonenzymatic antioxidant activities.* Food science & nutrition, 2019. **7**(5): p. 1555-1563.
140. Ferreira, C.A., et al., *Scavenging of reactive oxygen and nitrogen species with nanomaterials.* Nano research, 2018. **11**: p. 4955-4984.
141. Yin, J.-J., et al., *The scavenging of reactive oxygen species and the potential for cell protection by functionalized fullerene materials.* Biomaterials, 2009. **30**(4): p. 611-621.
142. Ionita, P., *The chemistry of DPPH· free radical and congeners.* International journal of molecular sciences, 2021. **22**(4): p. 1545.
143. Zhao, S., et al., *Green synthesis of bifunctional fluorescent carbon dots from garlic for cellular imaging and free radical scavenging.* ACS applied materials & interfaces, 2015. **7**(31): p. 17054-17060.
144. Chong, Y., et al., *Crossover between anti-and pro-oxidant activities of graphene quantum dots in the absence or presence of light.* ACS nano, 2016. **10**(9): p. 8690-8699.
145. Lin, J.-S., et al., *A carbon dot based theranostic platform for dual-modal imaging and free radical scavenging.* Nanoscale, 2019. **11**(43): p. 20917-20931.
146. Jovanović, S.P., et al., *Graphene quantum dots as singlet oxygen producer or radical quencher-The matter of functionalization with urea/thiourea.* Materials Science and Engineering: C, 2020. **109**: p. 110539.

147. Das, P., et al., *Immobilization of heteroatom-doped carbon dots onto nonpolar plastics for antifogging, antioxidant, and food monitoring applications.* Langmuir, 2021. **37**(11): p. 3508-3520.
148. Qiu, Y., et al., *Antioxidant chemistry of graphene-based materials and its role in oxidation protection technology.* Nanoscale, 2014. **6**(20): p. 11744-11755.
149. Ruiz, V., et al., *Tuning the antioxidant activity of graphene quantum dots: Protective nanomaterials against dye decoloration.* Carbon, 2017. **116**: p. 366-374.
150. Li, F., et al., *Selenium-doped carbon quantum dots for free-radical scavenging.* Angewandte Chemie International Edition, 2017. **56**(33): p. 9910-9914.
151. Su, R., et al., *Synthesis of ultrasmall and monodisperse selenium-doped carbon dots from amino acids for free radical scavenging.* Industrial & Engineering Chemistry Research, 2020. **59**(38): p. 16876-16883.
152. Rosenkrans, Z.T., et al., *Selenium-Doped Carbon Quantum Dots Act as Broad-Spectrum Antioxidants for Acute Kidney Injury Management.* Advanced Science, 2020. **7**(12): p. 2000420.
153. Zhou, D., et al., *Lysosome-targetable selenium-doped carbon nanodots for in situ scavenging free radicals in living cells and mice.* Microchimica Acta, 2021. **188**(7): p. 223.
154. Christensen, I.L., Y.-P. Sun, and P. Juzenas, *Carbon dots as antioxidants and prooxidants.* Journal of biomedical nanotechnology, 2011. **7**(5): p. 667-676.
155. Shin, Y., et al., *Mass production of graphene quantum dots by one-pot synthesis directly from graphite in high yield.* Small, 2014. **10**(5): p. 866-870.
156. González-González, R.B., et al., *Synthesis, purification, and characterization of carbon dots from non-activated and activated pyrolytic carbon black.* Nanomaterials, 2022. **12**(3): p. 298.
157. Wu, G., et al., *Oxidized activated charcoal nanoparticles as catalytic superoxide dismutase mimetics: evidence for direct participation of an intrinsic radical.* ACS Applied Nano Materials, 2020. **3**(7): p. 6962-6971.
158. Gao, W., et al., *Deciphering the catalytic mechanism of superoxide dismutase activity of carbon dot nanozyme.* Nature communications, 2023. **14**(1): p. 160.
159. Mäntele, W. and E. Deniz, *UV–VIS absorption spectroscopy: Lambert-Beer reloaded*. 2017, Elsevier. p. 965-968.